# Wall impact on efficiency of packed-bed thermocline thermal energy storage system

Baoshan Xie, Nicolas Baudin, Jérôme Soto, Yilin Fan, Lingai Luo

# Wall impact on efficiency of packed-bed thermocline thermal energy storage system

Baoshan XIE[1], Nicolas BAUDIN[1], Jérôme SOTO[1,2], Yilin FAN[1], Lingai LUO[1,*]

[1] *Nantes Université, CNRS, Laboratoire de thermique et énergie de Nantes, LTeN, UMR 6607, F-44000 Nantes, France*

[2]*Institut Catholique d'Arts et Métiers de Nantes, 35 avenue du Champ de Manœuvres, 44470 Carquefou, France*

**Abstract:** Packed-bed single-tank thermocline system with reduced cost is an alternative to the conventional two- tank system for thermal energy storage. This work systematically explores the wall impact on thermo- cline behavior of packed-bed tanks. For this purpose, adapted transient models were developed and fully exploited for the first time. Two tank configurations were investigated and compared: a high- temperature pilot-scale tank with a steel wall and a low-temperature lab-scale tank with a polycarbonate wall, both tanks being insulated by mineral wool. Results showed that the maximum energy stored in the wall at fully charged state can be up to 10% of the total stored energy. This part of stored energy has a negative impact on the discharging, causing up to 15% increase of the thermocline thickness. The energy stored in the insulation is very small so that this phase can be simplified as a thermal resistance in the modeling. The optimal wall parameters for packed-bed TES tanks were obtained that a thinner wall has a smaller impact on the energy and exergy efficiencies at the discharging cutoff time. The findings of study could provide useful design guideline for pack-bed thermocline TES tanks for different industrial applications.

**Keywords:** thermal energy storage; packed-bed; wall impact; thermocline; heat loss; modeling

* Corresponding author

Email address: lingai.luo@univ-nantes.fr (L. Luo)

## Nomenclature

| | |
|---|---|
| $a$ | Surface area per unit volume ($m^2\ m^{-3}$) |
| $A$ | Superficial area ($m^2$) |
| $Bi$ | Biot number, $Bi=h\cdot(V/A)/\lambda$ |
| $c$ | Coefficient |
| $C_p$ | Specific heat capacity ($J\ kg^{-1}\ K^{-1}$) |
| $D_p$ | Diameter of particle (m) |
| $E$ | Energy (J) |
| $E_x$ | Exergy (J) |
| $g$ | Acceleration due to gravity ($m\ s^{-2}$) |
| $Gr$ | Grashof number, $Gr=g\cdot\beta\cdot H^3\cdot\Delta T/\nu^2$ |
| $h$ | Heat transfer coefficient ($W\ m^{-2}\ K^{-1}$) |
| $H$ | Free height of packed-bed region (m) |
| $L$ | Layer thickness (m) |
| $\dot{m}$ | Mass flow rate ($kg\ s^{-1}$) |
| $N$ | Node, or slice number |
| $Nu$ | Nusselt number |
| $P$ | Power (W) |
| $\Delta P$ | Pressure drop (Pa) |
| $Pe$ | Peclet number, $Pe=D_p\cdot u_{sup}/\alpha$ |
| $Pr$ | Prandtl number, $Pr=C_p\cdot\mu/\lambda$ |
| $\dot{Q}$ | Heat flow (W) |
| $r$ | Radial coordinate |
| $Ra$ | Rayleigh number, $Ra= Gr\cdot Pr$ |
| $Re$ | Reynold number, $Re=(\rho_f\cdot D_p\cdot u_{sup})/\mu_f$ |
| $R_{int}$ | Internal radius of tank (m) |
| $R_{mid}$ | Middle radius of tank (m) |
| $R_{ext}$ | External radius of tank (m) |
| $t$ | Time (s) |
| $TR$ | Thermal resistance ($K\ W^{-1}$) |
| $T$ | Temperature (K) |
| $T_C$ | Coldest operation temperature of system (K) |
| $T_H$ | Highest operation temperature of system (K) |
| $T_{in}$ | Fluid inlet temperature (K) |
| $T_{out}$ | Fluid outlet temperature (K) |
| $u$ | Interstitial fluid velocity ($m\ s^{-1}$), $u=\dot{m}/(\rho_f\varepsilon\cdot\pi\cdot R_{int}^2)$ |
| $u_{sup}$ | Superficial fluid velocity ($m\ s^{-1}$), $u_{sup}=u\cdot\varepsilon$ |
| $V$ | Volume ($m^3$) |
| $St$ | Stanton number, $St=Nu/Pe$ |
| $z$ | Axial coordinate |

**Greek symbols**

| | |
|---|---|
| $\alpha$ | Thermal diffusivity ($m^2\ s^{-1}$), $\alpha= \lambda/ (\rho\cdot C_p)$ |
| $\lambda$ | Thermal conductivity ($W\ m^{-1}\ K^{-1}$) |
| $\sigma$ | Stefan-Boltzmann constant, $5.67\times10^{-8}$ ($W\cdot m^{-2}\cdot K^{-4}$) |
| $\varepsilon$ | Porosity |
| $\mu$ | Dynamic viscosity (Pa s) |
| $\rho$ | Density ($kg\ m^{-3}$) |
| $\epsilon$ | Emissivity |
| $\beta$ | Thermal expansion coefficient of air ($K^{-1}$) |
| $\eta$ | Energy efficiency |
| $\eta_x$ | Exergy efficiency |
| $\nu$ | Kinematic viscosity ($m^2\ s^{-1}$) |
| $\Pi_i$ | Dimensionless numbers |

**Subscripts**

| | |
|---|---|
| *amb* | Ambient |
| *ave* | Average |
| *b* | Packed bed region of inner diameter of tank |
| *cond* | Conductive |
| *conv* | Convective |
| *ch* | Charging |
| *disch* | Discharging |
| *diff* | Diffusivity |
| *eff* | Effective value |
| *ext* | External surface of tank |
| *f* | Fluid |
| *ini* | Initial |
| *ins* | Insulation |
| *int* | Internal surface of tank |
| *max* | Maximum |
| *mid* | Middle surface of tank |
| *mix* | Mixing |
| *o* | Overall value |
| *rad* | Radiative |
| *s* | Solid |
| *w* | Wall |

**Abbreviation**

| | |
|---|---|
| CSP | Concentrated Solar Power |
| D | Dimension |
| HTC | Heat Transfer Coefficient |
| HTF | Heat Transfer Fluid |
| P | Phase |
| RMS | Root Mean Square |
| SD | Standard Deviation |
| TES | Thermal Energy Storage |

## 1. Introduction

Integrating thermal energy storage (TES) system in the concentrated solar power (CSP) plant is a feasible and appropriate strategy to overcome the inherent fluctuation and intermittence of natural renewable energy sources and to improve the flexibility and dispatchability [1,2]. Without any fossil fuel backup, the CSP plant supported by TES is also capable of producing electricity continuously, showing the prospect to replace traditional thermal power plants in the future due to the highly cleanness and sustainability [3–5]. At present, TES candidates for CSP plant are commonly classified into three types according to the sensible, latent or thermochemical heat storage mechanism [6,7]. Among them, the sensible heat TES is a comparatively mature and predominant technology because of its low cost and design simplicity [3][8]. Latent and thermochemical TES systems having higher energy density also exhibit great potential in commercial-scale CSP plants in the future [9–13].

As for the possible configurations of the TES system, two-tank and single-tank systems have been developed [14]. In a two-tank system, hot and cold fluids are stored separately in their own high-/low-temperature tank [15]. Being the most widely used TES configuration, it offers a good balance of capacity, usability and stable output for large-scale CSP plants [16,17]. However, the utilization volume of the two-tank system is only around 50% in a full charging/discharging process [18], requiring thereby a significantly high investment cost of tank body and a high quantity of storage medium [19]. The single-tank thermocline system, where hot and cold fluids stay in the same tank but are separated by their density difference, is considered as a possible alternative for cost-reduction in industry [20,21]. Especially when low-cost fillers serve as a storage medium and the heat transfer fluid (HTF) flows through the packed bed region, the dual-media single-tank thermocline system can cut off the costs by 20-37% in comparison to a two-tank system [22,23].

The stratification zone, called the “thermocline”, is an area with an important temperature gradient between hot and cold fluids in single-tank TES system [24]. The thermocline thickness, which reflects the thermal efficiency of storage tank, is in fact hard to be maintained in stable condition during the charging/discharging operations [25]. Main causes of thermocline degradation include [16]: (1) heat convection between solid and fluid, (2) axial heat conduction between fillers, (3) heat transfer between HTF and wall/insulation, and (4) fluid flow adjacent to tank walls due to different local void fraction. To achieve higher thermal efficiency of the storage tank, it is critical to maintain the temperature stratification, to enhance the heat transfer between HTF and solid fillers and to reduce heat losses [26].

Wall heat impact is a heat transfer phenomenon that the HTF in near-wall region appears to be overheated/overcooled than that in central tank region due to various factors, including the heat loss from storage tank to ambient, the stored/released wall energy in charging/discharging and the different void fraction in near-wall region compared to the center. It is regarded to be responsible, to some extent, for the thermocline decay or instability and thus the reduced efficiency of the TES system.

Various studies have been done to investigate the wall impact or boundary conditions in packed-bed TES tanks [27]. Argo and Smith [28] conducted fundamental research on the effect of convective boundary layer in wall region on the temperature distribution of packed beds. By testing and comparing the temperature profiles in core region and near-wall region of a packed-bed tank with gas flow, their results showed that the temperature drop in near-wall region occurred. Chang et al. [3] further investigated the effect of physical boundary conditions including insert liner and sloped wall on the thermal performance of thermocline storage system by analyzing the entropy generation. It was observed that the thermocline thickness was larger and much more fluctuated in the near-wall area along the tank height than that in the center of the tank under the insert liner boundary condition. De Beer et al. [29] studied the influence of wall effects on the effective thermal conductivity in the near-wall region at different temperature levels and with different packing structures. A notable reduction of thermal conductivity of bed that separated into the inner and outer regions was found and the influence was more significant at high temperature. In summary, such wall effects are mainly caused by unevenly distributed fluid flow in the near-wall region, which can though be ignored/alleviated at low Reynolds numbers ($Re$) or using the effective thermal conductivity [30], and thus is not the main matter of concern for this study.

Another class of studies in the literature has focused on the heat loss and the stored/released heat in tank wall as well as in the insulation layer. Commonly three boundary types with increasing complexity have been used: (1) adiabatic boundary; (2) non-adiabatic boundary with heat loss and (3) non-adiabatic boundary with heat loss and with stored heat. The adiabatic/non-adiabatic boundary condition was usually adopted to simplify the model when heat loss to ambient was negligible or could be calculated using an overall wall heat transfer coefficient. For example, Yang and Garimella [31] compared the adiabatic and non-adiabatic boundary on the thermocline performance. It was found that the heat loss under non-adiabatic boundary distorted the flow temperature distributions, but such influence became insignificant at large flow $Re$. The discharge efficiency of the thermocline tank was found to increase with the increasing $Re$, opposite to the trend under adiabatic condition. Mira-Hernández et al. [32] reported that the heat loss under non-adiabatic condition could cause inhomogeneous internal flow for the whole tank due to the cooling of molten salt near the tank wall. But the total heat lost during charge/discharge the cycle was estimated to be negligible compared to the heat storage capacity. Nevertheless, when the wall volume (or mass) constitutes a large proportion of the whole storage system, the heat capacity of tank walls (including the insulation) has to be taken into account by adding the energy equation. In this regard, Beasley and Clark [33] have developed a 2D transient response model of both solid and fluid phases that includes the effects of longitudinal conduction, the stored heat in walls and the heat loss, with air as the working fluid. But the solid internal heat conduction term was neglected in this model. Xu et al. [34] developed a 2 dimension-2 phase (2D-2P) model with energy equations for the insulations and tank steel wall, and studied the effect of insulation on the thermocline behavior in a hypothetical high temperature utility-scale tank (14 m in

height). Their results showed that the increased insulation thickness could form a uniform temperature in the cross-section even through the temperature of HTF (molten salt) near the wall could be slightly influenced by the wall temperature. Hoffmann et al. [35] further proposed a model with three governing equations considering the wall as a third component in addition to solid and fluid phases. Their model, validated in different size tanks with liquid HTF, showed that the tank walls and the heat loss had a direct influence on the HTF outlet temperature for a pilot-scale tank. However, the radiation loss from the outer tank surface and the thermal resistance of the wall was not considered in their modeling. **Table 1** summarizes main features of previous studies on the issues of wall impacts in packed-bed thermocline TES systems.

The above literature survey indicates that even though previous works investigated the influence of non-adiabatic boundary on the thermal performance of packed-bed thermocline tank, the research gap still exists in the following points. Firstly, the effects of wall thermal properties on the dynamic thermocline behavior are not fully addressed. The total amount of stored heat in the wall (and insulation) phase and its influence on the efficiency of the storage tank need to be further evaluated as well. Secondly, besides the large-scale thermocline tanks applied to CSP plants at high temperature, thermocline tanks are also frequently used for waste heat recovery at medium temperature or for buildings at low temperature. For these applications, the size of the storage tanks is relatively small thus the tank wall and the insulation could occupy a relatively large volume ratio compared to the packed-bed region. It is thereby essential and necessary to explore wall impact on different size tanks to acquire a better understanding of system operation, especially the wall parameters. Thirdly, the trade-off between conflicting requirements that models correspond to different levels of detail and different calculation times has been rarely reported in the literature. Choosing a proper model to do such wall parametric study is equally important towards an optimal wall design for packed-bed TES tank.

In order to fill the above-mentioned research gap, the present study aims at developing adapted transient model(s) with balanced complex physical phenomena description and computation time to systematically explore the wall impact on the dynamic thermocline behavior of the packed-bed storage tanks. Main objectives of this study are as follows:

--to comprehend the impact of the wall thermal properties on the heat loss and on the thermal performance of packed-bed thermocline storage tank with different sizes and under different working temperatures;

--to identify the most influencing factors through the parametric and sensitivity analyses in order to provide design guidelines for packed-bed thermocline tank.

To do this, the heat transfer behavior inside the tank wall and the insulation layer should be fully modelled, by considering them as an individual phase with a certain thickness. The models to be developed are expected to be more complete than existing ones, by taking the wall thermal resistance

and the radiative heat loss into account. The study has been organized with the following steps. (1) Three transient models with different complexity level, namely 1D-2P model, 1D-3P model, and 1.5D-4P model, were first developed and validated by two experimental data sets from the literature. (2) The wall impact on the dynamic thermocline behavior was investigated with two size thermocline TES tanks, including a high-temperature pilot-scale tank and a low-temperature lab-scale tank. (3) The energy stored in wall and heat loss due to different factors were evaluated and quantified. (4) The main influencing factors of wall parameters (thermal conductivity and wall thickness) were identified through a sensitivity analysis. Their effects on the energy and exergy efficiencies of two tanks were analyzed using the chosen 1D-3P model with enough accuracy and fast computational speed. (5) Finally, the optimal combination of wall parameters were determined, providing additional insights on the design guidelines of packed-bed TES tank.

**Table 1.** Studies of walls impacts on packed-bed thermocline system.

| Study | Year | Dimensions (Fluid/Solid/Wall) | Methods | Wall impacts | | | Main findings |
|---|---|---|---|---|---|---|---|
| | | | | Heat loss from wall to ambient (Yes/No) | Wall energy storage (Yes/No) | Near wall void fraction singularity (Yes/No) | |
| Beasley and Clark [33] | 1984 | 2D/1D/1D | Num./Exp. | Yes | Yes | Yes | ● Effects of void fraction near the wall, wall heat capacity, and wall energy losses on dynamic response are identified. |
| Yang and Garimella [31] | 2010 | 2D/2D/-- | Num. | Yes | No | No | ● Heat loss for non-adiabatic boundary distorts the flow temperature distributions, but such influence becomes insignificant at large flow rate ($Re$>250). |
| Xu et al. [34] | 2012 | 2D/2D/2D | Num. | Yes | Yes | No | ● Insulation tends to reduce temperature difference in the cross-section of tank. |
| Bellan et al. [36] | 2014 | 2D/2D/-- | Num. | Yes | No | No | ● Heat loss through the wall increases with the decreasing insulation layer thickness, which is less than 1% of the inlet energy at a steady state. |
| Opitz and Treffinger [37] | 2014 | (1D,1D)/(1D,1D)/-- | Num. | Yes | No | Yes | ● A general heterogeneous model with two zones mean void fraction is from in the cross-section is developed and validated. |
| Mira-Hernández et al. [32] | 2015 | 2D/2D/-- | Num. | Yes | No | No | ● Heat loss under non-adiabatic conditions causes thermal-buoyancy-induced flow non-uniformities.<br>● Total heat loss during the cycle is negligible compared to the heat storage capacity. |
| Chang et al. [3] | 2016 | 2D/2D/-- | Num. | Yes | No | No | ● Thermocline thickness is much more fluctuated in the near-wall region along the tank height than that in the center of the tank. |
| Cascetta et al. [22] [38] | 2016 | 2D/2D/-- | Num./Exp. | Yes | Yes | Yes | ● Wall influences the radial temperature profile and the amount of the stored energy. |
| Hoffmann et al. [35] | 2016 | 1D;<br>1D/1D/1D<br>(No wall heat radiation) | Num. | Yes | Yes | No | ● 1D-1P model is faster but another model integrated different phases of fluid, solid, and wall is more accurate.<br>● Over 5% of the energy storage capacity, the wall needs to be considered. |
| Fernández-Torrijos et al. [25] | 2017 | 1D/1D/2D | Num. | Yes | Yes | No | ● With a wall Nusselt number ($Nu$) of about 102, an optimum value of fluid flow rate can maximize the overall energy efficiency and minimize the steel shell stress. |
| ELSihy et al. [39] | 2021 | 2D/2D/2D | Num. | Yes | Yes | No | ● Employing heat loss boundary condition causes a faster temperature drop of the HTF near the tank wall, forming a temperature gradient. |
| This study | 2022 | 1D/1D/--;<br>1D/1D/2D;<br>1D/1D/1D; | Num. | Yes | Yes | No | ● Wall impact comparison on two different scale tanks.<br>● Wall impact on thermocline behavior.<br>● Wall parametric studies to provide wall design guideline. |

## 2. Methodology

### 2.1. Geometry and assumptions

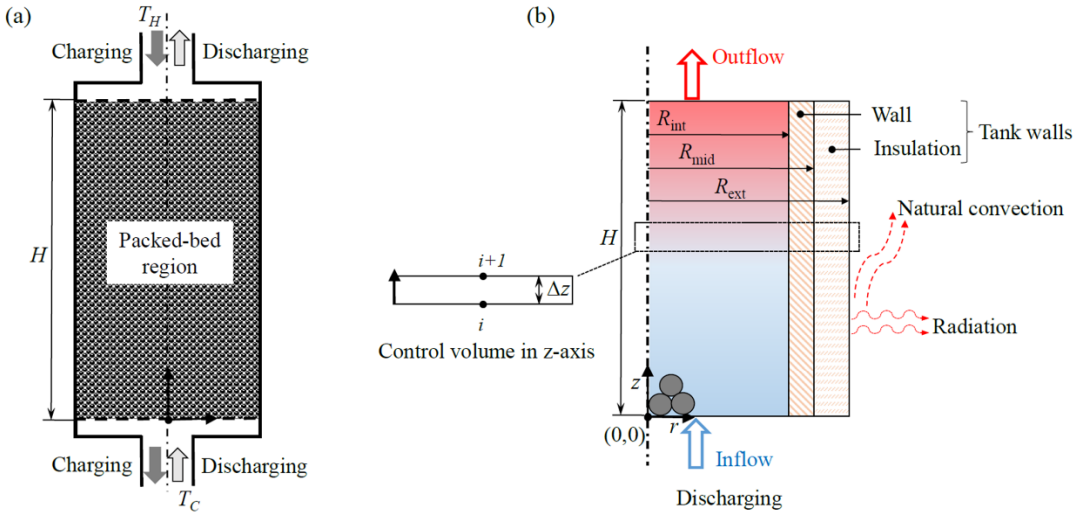


**Fig. 1.** Packed-bed thermocline TES tank. (a) schematic illustration; (b) computational domain in discharging process.

A typical structure of packed-bed thermocline TES tank and the computational domain are illustrated in **Fig. 1.** It is a vertical cylindrical tank with solid particles as heat storage medium to form the packed-bed thermal storage region (with a free height of $H$ and an internal radius of $R_{int}$). The HTF flows in void space of the region, the void fraction or porosity of packed-bed tank being defined as $\varepsilon = \frac{V_b - V_s}{V_b}$ where $V_s$ is the total volume of solid particles and $V_b$ is the whole tank volume based on inner tank diameter of $R_{int}$ and free height of $H$ [40]. The packed-bed cylindrical tank has an inner wall to form the tank and an outer insulation to prevent heat loss. These two layers constitute a composite wall called 'tank walls' in the following text. Furthermore, the inlet and outlet ports are openings at the top and bottom of the tank, allowing HTF to flow in and out the tank. In charging or thermal storage stage, the hot HTF at the highest operation temperature ($T_H$) flows into the TES tank from the top port to transfer heat to low-temperature solid medium, and then flows out from the bottom port. Conversely, in discharging or thermal release stage, the cold HTF with the coldest temperature ($T_C$) enters from the tank bottom to absorb heat from high-temperature solid medium and flows out of tank from the top port.

To simplify the model formulation and analysis, following assumptions have been employed:

(1) Inlet temperature and inlet/outlet mass flow rate of HTF are constant in charging and discharging processes.

(2) Bottom and top surfaces of the tank are adiabatic and there is no internal heat generation in the bed. The contact thermal resistance between wall and insulation is neglected.

(3) Thermal conduction and radiation between solid fillers are neglected as well as the heat transfer between solid particles and wall, due to the point contact.

(4) The thermo-physical properties of HTF and solid fillers are considered as constant and determined by an average operating temperature: $T_{ave} = \left(\frac{T_H+T_C}{2}\right)$.

(5) HTF is assumed as incompressible fluid and plug flow (in $z$-axis direction). Solid fillers are identical and isotropic spherical particles with homogeneous temperature.

When the temperature inside a particle varies significantly in space coordinate, the internal heat conduction resistance cannot be ignored. This assumption is named as a lumped capacitance that is valid when the value of the Biot number of solid ($Bi_s = \frac{h_{sf} \cdot D_p}{6 \cdot \lambda_s}$) is smaller than 0.1 [41,42]. Even the $Bi_s$ in this work ranges between 0.2 and 0.28, the temperature gradient inside particle is neglected by introducing an effective heat transfer coefficient (HTC) between solid and fluid [43,44].

## 2.2. Numerical models

In this work, three transient numerical models with different dimensions and phases, fluid, solid fillers, wall, or insulation phase, are studied: a $z$-axis 1D-2P model (fluid-solid), a $z$-axis 1D-3P model (fluid-solid-wall), and a 1.5D-4P model (1D $z$-axis for fluid-solid, 2D $z$-axis and $r$-axis for wall-insulation) that 1.5D refers to the average of 1D and 2D. **Fig. 2** shows the research process and the relationship between models. At first, models were compared and validated by experimental data sets. Further, the wall thermal behavior for two different scale tanks was investigated by using a complicated model (1.5D-4P). After that, an appropriate model (1D-3P) is selected to conduct parametric sensitivity analysis and wall parametric study.

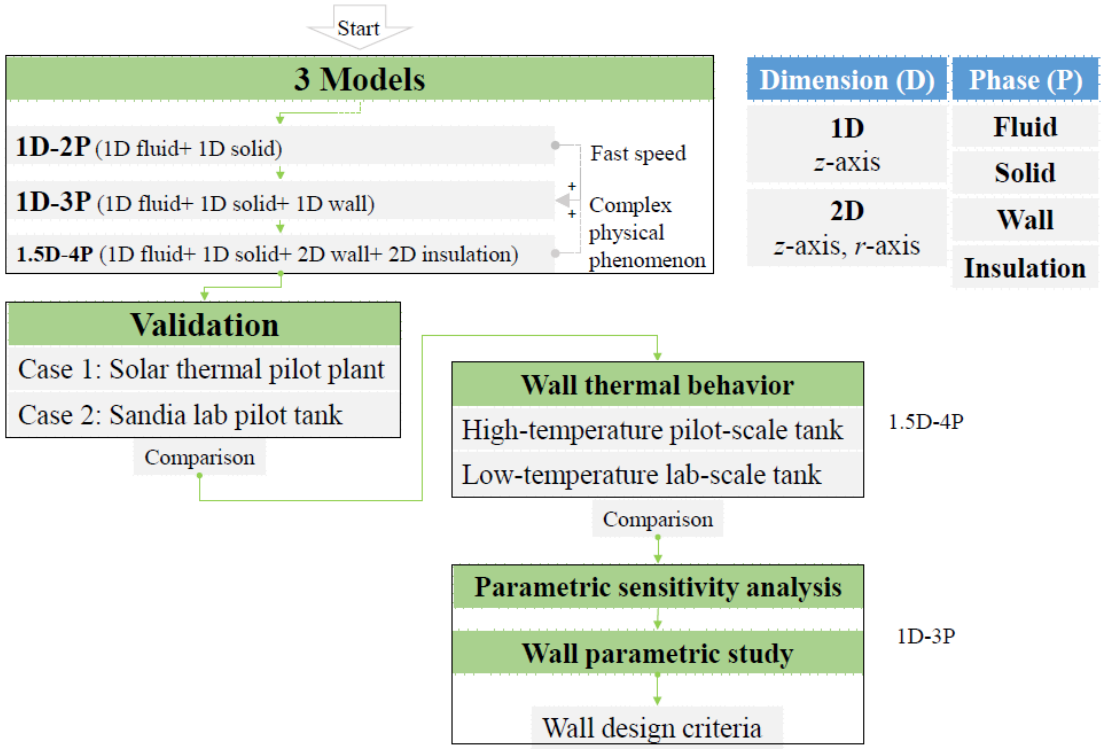


**Fig. 2.** Diagram of the research process in this study.

### 2.2.1. One-dimensional two-phase model (1D-2P)

A 1D-2P model, or Schumann's model, is introduced to perform fast simulation. In this model, only fluid and solid filler material are modeled using an averaged porous model while the walls are not included. Governing equations of the control volume for two phases and corresponding correlations can be written as follows.

- **Governing equations**

Fluid:

$$\varepsilon \cdot \rho_f \cdot C_{p_f} \cdot \left(\frac{\partial T_f}{\partial t} + u_f \cdot \frac{\partial T_f}{\partial z}\right) = \frac{\partial}{\partial z} \cdot \left(\lambda_{f,eff} \cdot \frac{\partial T_f}{\partial z}\right) + h_{sf,eff} \cdot a_s \cdot \left(T_s - T_f\right) + h_o \cdot a_b \cdot \left(T_{amb} - T_f\right) \quad (1a)$$

Solid:

$$(1-\varepsilon) \cdot \rho_s \cdot C_{p_s} \cdot \frac{\partial T_s}{\partial t} = \frac{\partial}{\partial z} \cdot \left(\lambda_{s,eff} \cdot \frac{\partial T_s}{\partial z}\right) + h_{sf,eff} \cdot a_s \cdot \left(T_f - T_s\right) \quad (1b)$$

where the porosity ($\varepsilon$), density ($\rho$), specific heat capacity ($C_p$), particle diameter ($D_p$) and internal radius of tank ($R_{int}$) are constants used in equations. The subscript *f*, *s*, *b*, *o*, *eff*, and *amb* represents the fluid, solid, packed-bed region, overall value, effective value, and ambient, respectively. $a_s = \frac{6\cdot(1-\varepsilon)}{D_p}$ and $a_b = \frac{A_b}{V_b} = \frac{2}{R_{int}}$ are the shape factor for solid particles and for the cylindrical tank, respectively. The interstitial fluid velocity ($u_f$) is calculated based on the mass flow rate: $\dot{m}_f = u_f \cdot \rho_f \cdot \varepsilon \cdot \pi \cdot R_{int}^2$.

**● Effective thermal conductivity for fluid and solid**

The heat transfer of the fluid phase takes into account the thermal diffusion in stagnant fluid and the turbulent thermal contribution in fluid mixing. Thus, the effective thermal conductivities for each fluid ($\lambda_{f,eff}$) and solid phase ($\lambda_{s,eff}$) are given as:

$$\lambda_{f,eff} \cong (\varepsilon \cdot \lambda_f + c \cdot \lambda_f) + \lambda_{mix} \tag{2a}$$

$$\lambda_{s,eff} \cong [(1-\varepsilon) \cdot \lambda_s - c \cdot \lambda_s] \tag{2b}$$

where $\lambda_{mix} = 0.5 \cdot Re \cdot Pr \cdot \lambda_f$ is the fluid mixing turbulent contribution based on Wakao and Kaguei's empirical correlation for $Re$>0.8 [45,46]. Besides, a coefficient ($c$) covering the geometry tortuosity of the packed-bed with parallel packing condition is introduced [47,48].

$$c \cong \frac{\lambda_{eff}^0 - \varepsilon\cdot\lambda_f - (1-\varepsilon)\cdot\lambda_s}{\lambda_f - \lambda_s} \tag{2c}$$

$$\lambda_{eff}^0 = \left[\frac{1+2\cdot\alpha\cdot(1-\varepsilon)+(2\cdot\alpha^3-0.1\cdot\alpha)\cdot(1-\varepsilon)^2+(1-\varepsilon)^3\cdot 0.05\cdot\exp(4.5\cdot\alpha)}{1-\alpha\cdot(1-\varepsilon)}\right]\cdot\lambda_f \tag{2d}$$

$$\alpha = (\lambda_s - \lambda_f)/(\lambda_s + 2\cdot\lambda_f) \tag{2e}$$

where $\lambda_{eff}^0$ is the thermal conductivity contribution of both phase in stagnant condition with the valid range of 0.15<$\varepsilon$<0.85, and $10^{-3}$<$\lambda_s/\lambda_f$<$10^4$ [48].

**● Effective HTC between solid and fluid**

The forced convection and natural convection contribute dissimilarly to the heat transfer between fluid and solid [49]. The solid-to-fluid HTC ($h_{sf}$) from Pfeffer is given as [50]:

$$h_{sf} = \left(\frac{\lambda_f}{D_p}\right)\cdot\left\{1.26\cdot\left[\frac{1-(1-\varepsilon)^{\frac{5}{3}}}{2-3\cdot(1-\varepsilon)^{\frac{1}{3}}+3\cdot(1-\varepsilon)^{\frac{5}{3}}-2\cdot(1-\varepsilon)^2}\cdot Re\cdot Pr\right]^{\frac{1}{3}}\right\}, \quad (Re<74) \tag{3a}$$

Moreover, in order to approach the assumption of uniform temperature inside the solid particle, or to extend the applicability of lumped capacitance method when $Bi_s$>0.1, the solid-to-fluid effective HTC ($h_{sf,eff}$) through the method of weight average time (or the effective average time [51]) is used [42]:

$$h_{sf,eff} = \frac{1}{1/h_{sf}+3\cdot Bi_s/m} \tag{3b}$$

where the value of $m$ equal to 5, 4, and 3 for different shapes of sphere, cylinder and slab (cube), respectively.

**● Overall HTC through tank walls**

The overall HTC through tank walls ($h_o$) based on the inner surface area is calculated by:

$$\frac{1}{h_o} = \frac{1}{h_{int}} + \left[\frac{1}{\lambda_w} ln\left(\frac{R_{mid}}{R_{int}}\right) + \frac{1}{\lambda_{ins}} ln\left(\frac{R_{ext}}{R_{mid}}\right)\right] \cdot R_{int} + \frac{1}{h_{ext}+h_{rad}} \cdot \frac{R_{int}}{R_{ext}} \tag{4}$$

The fluid-to-wall convective HTC ($h_{int}$) on internal or inner surface is determined according to the empirical correlation of Yagi and Wakao [30]:

$$h_{int} = \left(\frac{\lambda_f}{H}\right) \cdot 0.6 \cdot Re^{1/2} \cdot Pr^{1/3} \quad (1<Re<40) \tag{5a}$$

The insulation-to-ambient air convective HTC ($h_{ext}$) on external or outer surface is calculated by a correlation of natural convection on vertical standing wall given by VDI-Wärmeatlas [52]:

$$h_{ext} = \left(\frac{\lambda_{air}}{H}\right)\left\{0.825 + \frac{0.387\cdot Ra_{air}^{1/6}}{\left[1+(0.492/Pr_{air})^{9/16}\right]^{8/27}}\right\}^2 \qquad (Ra_{air}<10^{12}) \tag{5b}$$

where $\lambda_w$ and $\lambda_{ins}$ is the wall and insulation thermal conductivity, respectively. $Ra$ is the Rayleigh number ($Ra_{air} = Gr_{air} \cdot Pr_{air}$), $Gr$ is the Grashof number ($Gr_{air} = \frac{g\cdot\beta\cdot H^3\cdot\Delta T}{v^2}$), and $\Delta T$ is the temperature difference between the outer surface and the ambient air. $g$, $\beta$, and $v$ stands for the acceleration of gravity, the thermal expansion coefficient of air, and the kinematic viscosity of air, respectively.

The radiative HTC ($h_{rad}$) based on the Stefan–Boltzmann law can be written:

$$h_{rad} = \frac{\epsilon\cdot\sigma\cdot\left[(T^4(\mathrm{K})-T_{amb}^4\right]}{T-T_{amb}} \tag{5c}$$

where ϵ is the emissivity factor is taken to 0.95, and $\sigma$=5.67×10$^{-8}$ W·m$^{-2}$·K$^{-4}$ is the Stefan-Boltzmann constant. $T$ here is defined as the outer surface temperature of the insulation calculated at average operation temperature $T_{ave}$, using the iterative method in advance.

### 2.2.2. One-dimensional three-phase model (1D-3P)

A modified 1D-3P model was developed by considering the tank wall as a separate phase in addition to the fluid and solid phases. In this way, the energy balance and the heat capacity of the tank wall are considered in 1D (z-axis direction). The insulation is simplified by a thermal resistance while its heat capacity is neglected due to the small temperature variation.

● **Governing equations**

Fluid:

$$\varepsilon \cdot \rho_f \cdot C_{p,f} \cdot \left(\frac{\partial T_f}{\partial t} + u_f \cdot \frac{\partial T_f}{\partial z}\right) = \frac{\partial}{\partial z} \cdot \left(\lambda_{f,eff} \cdot \frac{\partial T_f}{\partial z}\right) + h_{sf,eff} \cdot a_s \cdot (T_s - T_f) + h_{f-w} \cdot a_f \cdot (T_w - T_f) \quad (6a)$$

Solid:

$$(1-\varepsilon) \cdot \rho_s \cdot C_{p,s} \cdot \frac{\partial T_s}{\partial t} = \frac{\partial}{\partial z} \cdot \left(\lambda_{s,eff} \cdot \frac{\partial T_s}{\partial z}\right) + h_{sf,eff} \cdot a_s \cdot (T_f - T_s) \quad (6b)$$

Wall:

$$\rho_w \cdot C_{p,w} \cdot \frac{\partial T_w}{\partial t} = \frac{\partial}{\partial z} \cdot \left(\lambda_w \cdot \frac{\partial T_w}{\partial z}\right) + h_{f-w} \cdot a_w \cdot (T_f - T_w) + h_{w-amb} \cdot a_w \cdot (T_{amb} - T_w) \quad (6c)$$

where $a_f = \frac{A_{f-w}}{V_b} = \frac{R_{int}+R_{mid}}{R_{int}^2}$ and $a_w = \frac{A_{f-w}}{V_w} = \frac{R_{int}+R_{mid}}{R_{mid}^2-R_{int}^2}$ are the shape factor for fluid-wall surface to packed-bed volume and fluid-wall surface to wall volume, respectively.

The wall temperature ($T_w$) is defined as the temperature at the average diameter $\left(\frac{R_{int}+R_{mid}}{2}\right)$ of the tank wall. The equivalent HTC of fluid-to-wall center ($h_{f-w}$) and the equivalent HTC of wall center-to-ambient ($h_{w-amb}$) can be formulated as:

$$\frac{1}{h_{f-w}} = \frac{1}{h_{int}} + \frac{1}{\lambda_w} \cdot ln\frac{R_{int}+R_{mid}}{2 \cdot R_{int}} \cdot R_{int} \quad (7)$$

$$\frac{1}{h_{w-amb}} = \left[\frac{1}{\lambda_w} \cdot ln\left(\frac{2 \cdot R_{mid}}{R_{int}+R_{mid}}\right) + \frac{1}{\lambda_{ins}} \cdot ln\left(\frac{R_{ext}}{R_{mid}}\right) + \frac{1}{h_{ext}+h_{rad}} \cdot \frac{1}{R_{ext}}\right] \cdot R_{int} \quad (8)$$

### 2.2.3. One and half-dimensional four-phase model (1.5D-4P)

A 1.5D-4P model was used to explore the thermal behavior inside of the whole tank walls. In this model, the heat transfer in z-axis and r-axis for the wall and insulation occurs, and the different HTCs and effective thermal conductivities are calculated as defined before. It bases on full resolution and shows even more accuracy than the former two models.

● **Governing equations**

Fluid:

$$\varepsilon \cdot \rho_f \cdot C_{p,f} \cdot \left(\frac{\partial T_f}{\partial t} + u_f \cdot \frac{\partial T_f}{\partial z}\right) = \frac{\partial}{\partial z} \cdot \left(\lambda_{f,eff} \cdot \frac{\partial T_f}{\partial z}\right) + h_{sf,eff} \cdot a_s \cdot \left(T_s - T_f\right) + h_{int} \cdot a_b \cdot \left(T_{w,int} - T_f\right) \quad (9a)$$

Solid:

$$(1-\varepsilon) \cdot \rho_s \cdot C_{p,s} \cdot \frac{\partial T_s}{\partial t} = \frac{\partial}{\partial z} \cdot \left(\lambda_{s,eff} \cdot \frac{\partial T_s}{\partial z}\right) + h_{sf,eff} \cdot a_s \cdot \left(T_f - T_s\right) \quad (9b)$$

Wall:

$$\rho_w \cdot C_{p,w} \cdot \frac{\partial T_w}{\partial t} = \frac{\partial}{\partial z} \cdot \left(\lambda_w \cdot \frac{\partial T_w}{\partial z}\right) + \frac{\lambda_w}{r} \cdot \frac{\partial}{\partial r} \cdot \left(r \cdot \frac{\partial T_w}{\partial r}\right) \quad (9c)$$

Insulation:

$$\rho_{ins} \cdot C_{p,ins} \cdot \frac{\partial T_{ins}}{\partial t} = \frac{\partial}{\partial z} \cdot \left(\lambda_{ins} \cdot \frac{\partial T_{ins}}{\partial z}\right) + \frac{\lambda_{ins}}{r} \cdot \frac{\partial}{\partial r} \cdot \left(r \cdot \frac{\partial T_{ins}}{\partial r}\right) \quad (9d)$$

where the subscript "*ins*" represents the insulation phase.

### 2.2.4. Initial and boundary conditions

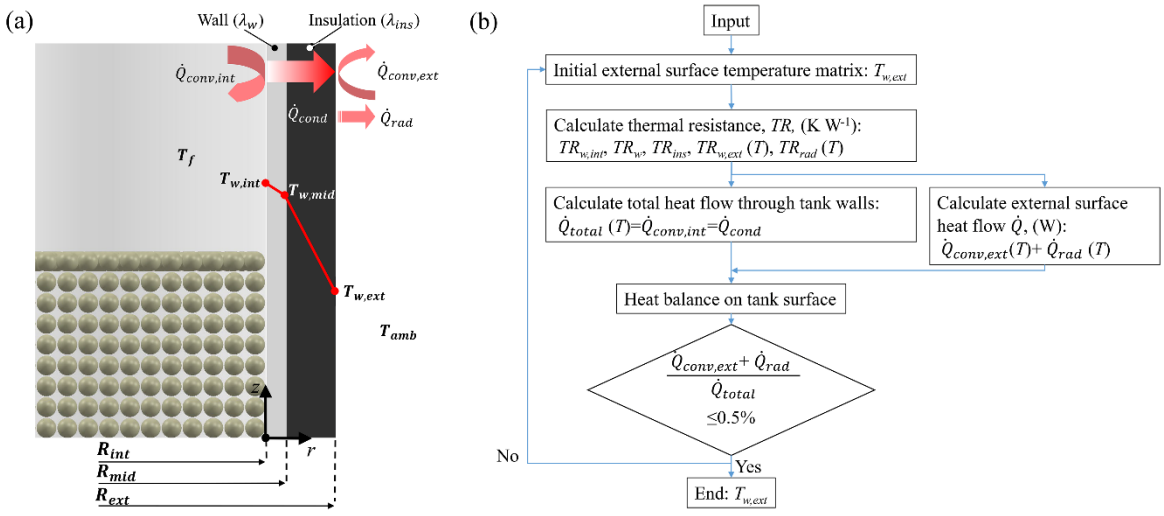

**Fig. 3.** Initial and boundary conditions for the modeling of discharging operation. (a) heat transfer through the wall and insulation at steady standby state ($T_{w,int}$, $T_{w,mid}$, and $T_{w,ext}$ is the temperature on inner, middle, and outer surface of tank, respectively); (b) iterative calculation to determine the initial outer surface temperature of fully charged tank before discharging.

In this work, only the discharging process was simulated and discussed. The initial conditions are given as:

$$T_s(t=0) = T_f(t=0) = T_{ini} = T_H \tag{10a}$$

$$T_{w,int}(t=0) = T_{w,int,ini},\ T_{w,mid}(t=0) = T_{w,mid,ini},\ T_{w,ext}(t=0) = T_{w,ext,ini} \tag{10b}$$

The initial temperature of tank walls ($T_{w,int,ini}$; $T_{w,mid,ini}$; $T_{w,ext,ini}$) before discharging is calculated by the fully charged tank temperature at the standby process using the iteration method as explained in **Fig. 3**. Note that the initial wall temperature ($T_{w,ini}$) in 1D-3P model is the average value of inner and middle surface temperature of wall.

The top and bottom boundary conditions of the tank for the computational domain shown in **Fig. 1b** are adiabatic. The HTF flows into the tank at the lowest operating temperature ($T_C$):

**BC1**: at the bottom inlet,

$$T_f(z=0) = T_C,\ \left.\frac{\partial T_s}{\partial z}\right|_{z=0} = \left.\frac{\partial T_w}{\partial z}\right|_{z=0} = \left.\frac{\partial T_{ins}}{\partial z}\right|_{z=0} = 0 \tag{11a}$$

**BC2:** at the top outlet,

$$\left.\frac{\partial T_f}{\partial z}\right|_{z=H} = \left.\frac{\partial T_s}{\partial z}\right|_{z=H} = \left.\frac{\partial T_w}{\partial z}\right|_{z=H} = \left.\frac{\partial T_{ins}}{\partial z}\right|_{z=H} = 0 \tag{11b}$$

In 1.5D-4P model, the boundary conditions at interfaces are added as:

**BC3 for 1D-2P model:** at the inner surface between wall and fluid,

$$h_{int} \cdot \left(T_{w,int} - T_f\right) = \lambda_w \cdot \left.\frac{\partial T_w}{\partial r}\right|_{r=R_{int}} \tag{12a}$$

**BC4 for 1D-3P model**: at the middle surface between wall and insulation,

$$\lambda_w \cdot \left.\frac{\partial T_w}{\partial r}\right|_{r=R_{mid}} = \lambda_{ins} \cdot \left.\frac{\partial T_{ins}}{\partial r}\right|_{r=R_{mid}} \tag{12b}$$

**BC5 for 1.5D-4P model:** at the outer surface between insulation and ambient,

$$\lambda_{ins} \cdot \frac{\partial T_{ins}}{\partial r}\Big|_{r=R_{ext}} = (h_{ext} + h_{rad}) \cdot \left(T_{amb} - T_{w,ext}\right) \quad (12c)$$

### 2.2.5. Performance indicators

- **Energy efficiency**

For a given time, the discharging energy efficiency ($\eta_{disch}$) is expressed as the ratio of energy accumulatively released ($E_{released}$) to initially stored in the tank ($E_{stored}$):

$$\eta_{disch} = \frac{E_{released}}{E_{stored}} \quad (13)$$

$$E(t)_{released} = \int_0^t \dot{m}_f \cdot C_{p,f} \cdot (T(t)_{out} - T_{in})dt \quad (14a)$$

$$E_{stored} = E_{f,stored} + E_{s,stored} + E_{w,stored} + E_{ins,stored} \quad (14b)$$

The consumed pumping energy for a given time in discharging is expressed as:

$$E_{pump} = \int_0^t \left(\dot{m}_f/\rho_f \cdot \Delta P\right)dt \quad (15)$$

where $\Delta P$ of packed-bed tank is calculated by Ergun equation [53]:

$$\frac{\Delta P}{H} = A \cdot \frac{(1-\varepsilon)^2}{\varepsilon^3} \cdot \frac{\mu_f \cdot u_{sup}}{D_{p,ave}^2} + B \cdot \frac{(1-\varepsilon)}{\varepsilon^3} \cdot \frac{\rho_f \cdot u_{sup}^2}{D_{p,ave}} \quad (16)$$

where $u_{sup}$ is the superficial fluid velocity, the values of A and B depend on the variation of $\varepsilon$ [54].

- **Exergy efficiency**

For a given time, the discharging exergy efficiency ($\eta_{x,disch}$) (or second law efficiency) is the ratio of the exergy of outlet fluid released from the bed ($\Delta E_{x,released}$) at a certain time to the exergy difference of all phases in packed bed before discharging ($\Delta E_{x,stored}$):

$$\eta_{x,disch} = \frac{\Delta E_{x,released}}{\Delta E_{x,stored}} \quad (17)$$

$$\Delta E_{x,released} = \int_0^t \dot{m}_f \cdot C_{p,f} \cdot \left[(T_{out} - T_{in}) - T_0 \cdot \ln\left(\frac{T_{out}}{T_{in}}\right)\right] dt \quad (18a)$$

$$\Delta E_{x,stored} = \Delta E_{x,f,stored} + \Delta E_{x,s,stored} + \Delta E_{x,w,stored} + \Delta E_{x,ins,stored} \quad (18b)$$

The reference temperature $T_0$ is selected as ambient temperature ($T_{amb}$) in this study.

- **Dimensionless parameters**

To be able to compare different tank configurations and working conditions, the variables are nondimensionalized as temperature ($T^*$), time based on flow velocity ($t^*$), time based on energy ($t_E^*$), height ($z^*$), radius ($r^*$), wall thickness ($L_w^*$) and wall thermal conductivity ($\lambda_w^*$):

$$T^* = \frac{T-T_C}{T_H-T_C}, \quad t^* = \frac{t \cdot u_f}{H}, \quad t_E^* = t \cdot \frac{\dot{m}_f \cdot c_p \cdot (T_H-T_C)}{E_{stored}}, \quad z^* = \frac{z}{H}, \quad r^* = \frac{r}{R_{int}}, \quad L_w^* = \frac{L_w}{R_{int}}, \quad \lambda_w^* = \frac{\lambda_w}{\lambda_f} \quad (19)$$

Here, $T_{out}{}^*$=0.2 was served as a given threshold value in discharging, corresponding to the discharging cutoff time when the outlet temperature reaches this value. The dimensionless thermocline thickness ($L_{thermocline}^*$) is defined as the covering length of the thermocline region [55] before reaching the tank top:

$$L_{thermocline}^* = \frac{z[T=T_H-0.05\cdot(T_H-T_C)]-z[T=T_C+0.05\cdot(T_H-T_C)]}{H}, \quad z[T = T_H - 0.05 \cdot (T_H - T_C)] < H \quad (20)$$

## 2.3. Model validation

The models were solved with the MATLAB function ode45 for the time derivatives. The explicit Runge Kutta (4.5) method was used with an adaptive time step. The advection term was discretized with a first order upwind finite difference, and the diffusion term was discretized with a second order central finite difference. The computational domain of numerical simulation was discretized into non-overlapping control volumes as illustrated in **Fig. 1b.** To obtain accurate simulation results and reduce the consumption of time, the reasonable node number ($N$) in z-axis was determined by using the cutoff time as an indicator of stable solution.

### 2.3.1. Cases description

Three cases with different scales, including two real tanks and a hypothetical lab-scale tank, are introduced. **Table 2** shows the characteristics and parameters of those three packed-bed TES tanks. **Table 3** summarizes the thermo-physical properties for HTF, solid fillers, and tank body materials**.** The first case widely used for model validation [35,56,57] is a 10 $MW_e$ packed-bed TES tank for a solar thermal power plant in which Caloria HT 43 is used as HTF under the operating temperature range of 179.2-295.5 °C [58,59]. The second case is a 2.3 $MWh_t$ packed-bed pilot-scale molten salt TES tank from Sandia lab provided by Pacheco et al. [60], with an operating temperature range of 290-390 °C. The molten salt used is a mixture of 60 wt% $NaNO_3$ and 40 wt% $KNO_3$. At last, a hypothetical lab-scale

TES water tank with a smaller size and lower temperature range of 20-75 °C is introduced to simulate the thermal performance under different operations. The ambient temperature of 20 °C was set as a reference for all cases.

**Table 2.** Operational and geometric parameters of packed-bed TES tanks.

| Parameters | Units | Solar thermal pilot plant tank [35,58,59] | Sandia laboratory pilot-scale tank [60] | Hypothetical lab-scale tank |
|---|---|---|---|---|
| HTF | -- | Caloria Ht-43 | Molten salt | Water |
| Solid filler | -- | Granite rock and sand | Quartzite rock and sand | Quartzite rock and sand |
| Tank height ($H$) | m | 12.0 | 6.0 | 0.4 |
| Tank middle radius ($R_{mid}$) | m | 9.10 | 1.50 | 0.11 |
| Thickness of wall ($L_w$) | m | 0.10 | 0.04 | 0.01 |
| Thickness of insulation ($L_{ins}$) | m | 0.20 | 0.20 | 0.04 |
| Porosity ($\varepsilon$) | -- | 0.22 | 0.22 | 0.22 |
| Free volume of packed bed ($V_b$) | $m^3$ | 3053.60 | 40.20 | $12.56\times10^{-3}$ |
| Particle diameter ($D_p$) | m | $4.61\times10^{-3}$ | $19.05\times10^{-3}$ | $5.00\times10^{-3}$ |
| HTF mass flow rate ($\dot{m}_f$) | kg $s^{-1}$ | 23.00 | 5.46 | $8.30\times10^{-3}$ |
| $T_H/T_C$ | °C | 295.2/179.2 | 390/290 | 75/20 |
| Wall materials | -- | Steel wall(ASTM 537 class 2) | Steel wall | Polycarbonate wall |
| Insulation | -- | Mineral wool | Mineral wool | Mineral wool |
| Discharging time | h | 8.0 | 3.0 | 0.5 |
| Spatial node in height | -- | 200 | 200 | 200 |

**Table 3.** Thermophysical properties of HTF, solid fillers and tank body materials.

| Solid fillers | $\rho_s$ (kg $m^{-3}$) | $C_{p,s}$ ( J $kg^{-1}$ $K^{-1}$) | $\lambda_s$ (W $m^{-1}$ $K^{-1}$) | $\rho_s \cdot C_{p,s}$ (kJ $m^{-3}$ $K^{-1}$) | Ref. |
|---|---|---|---|---|---|
| Granite rock and sand | 2643 | 1020 | 2.20 | 2696 | [56] |
| Quartzite rock and sand | 2500 | 830 | 5.69 | 2075 | [34] |
| Soda-lime glass | 2400 | 760 | 1.00 | 1824 | [61] |
| Tank body materials | $\rho_w$ (kg $m^{-3}$) | $C_{p,w}$ ( J $kg^{-1}$ $K^{-1}$) | $\lambda_w$ (W $m^{-1}$ $K^{-1}$) | $\rho_w \cdot C_{p,w}$ (kJ $m^{-3}$ $K^{-1}$) | |
| Steel wall(ASTM 537 class 2) | 7850 | 475 | 47.00 | 3728 | [57] |
| Steel wall | 7800 | 470 | 35.00 | 3666 | [34] |
| Polycarbonate wall | 1200 | 1170 | 0.20 | 1404 | -- |
| Insulation of mineral wool | 70*1 | 960 | 0.036 | 67.2 | [15] |
| Fluids | $\rho_f$ (kg $m^{-3}$) | $C_{p,f}$ ( J $kg^{-1}$ $K^{-1}$) | $\lambda_f$ (W $m^{-1}$ $K^{-1}$) | $\mu$ (Pa s) | |
| Caloria HT-43 (237.2 °C) | 701 | 2700 | 0.16 | $7.6\times10^{-4}$ | [35] |
| 60 wt% $NaNO_3$ and 40 wt% $KNO_3$ (340 °C) | 1874 | 1502 | 0.51 | $2.5\times10^{-3}$ | [34,62] |
| Water (47.5 °C) | 990 | 4187 | 0.634 | $5.8\times10^{-4}$ | [63,64] |

*1 It means the bulk density.

## 2.3.2. Validation results

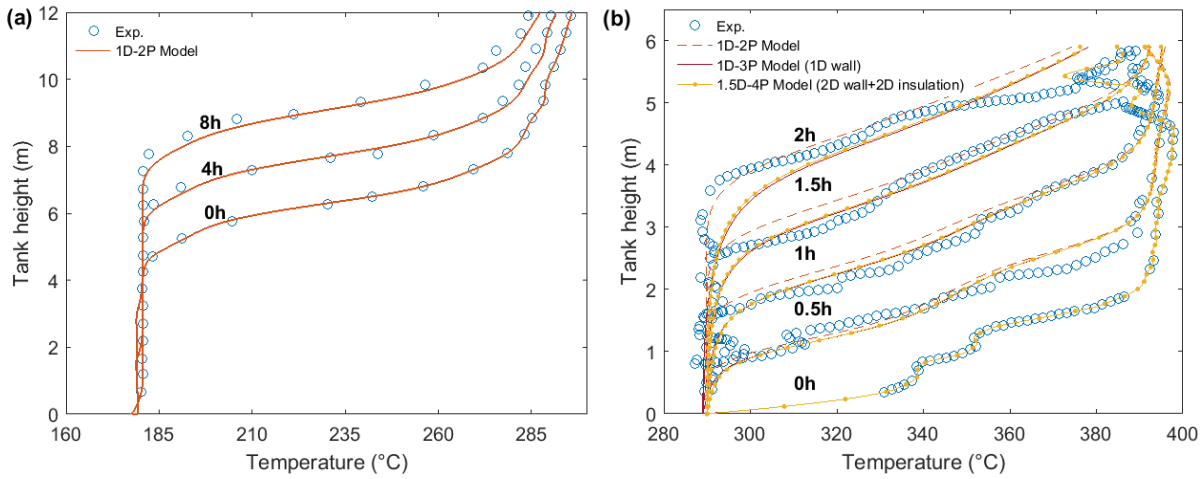


**Fig. 4.** Comparison of axial temperature evolution curves in discharging process between numerical results and experimental data. (a) solar power plant [58,59]; (b) Sandia pilot-scale tank [60].

**Table 4.** Difference between experimental and numerical results of the Sandia pilot-scale tank [60] for different models: mean difference for different times 0, 0.5, 1, 1.5, and 2h.

| Models | Average difference ($\overline{\Delta T}$, K) | Maximum difference ($\Delta T_{max}$, K) | Standard Deviation *1 (SD, K) | Root Mean Square difference *2 (RMS, K) |
|---|---|---|---|---|
| 1D-2P | 2.91 | 12.7 | 2.80 | 4.06 |
| 1D-3P | 3.63 | 12.5 | 3.44 | 5.02 |
| 1.5D-4P | 3.56 | 12.3 | 3.40 | 4.93 |

*1 The standard deviation (SD) at certain time along tank height is: $SD\ (t) = \sqrt{\frac{1}{N}\sum_{i=1}^{N}(\Delta T(i,t) - \overline{\Delta T(i,t)})^2}$, where $\Delta T(z,t) = |T_{exp.} - T_{num.}|$.

*2 The root mean square difference (RMS) at certain time along tank height is: $RMS\ (t) = \sqrt{\frac{1}{N}\sum_{i=1}^{N}[T_{exp.}(i,t) - T_{num.}(i,t)]^2}$

Fig. 4 shows the comparisons between numerical results and experimental data for axial temperature evolution curves of packed bed TES tanks in discharging. The measured experimental temperature profile at 0h was used as the initial temperature profile in the modeling to have the same beginning. The standard deviation (SD) and root mean square (RMS) of temperature difference between experiment and simulation results were calculated to evaluate the agreement degree.

Fig. 4a shows the validation results of 1D-2P model using the measured data from the solar thermal power plant tank ($Bi_s$=0.1). It is found that the simulated temperature profiles at 4h to 8h are generally

consistent with the experimental data considering that the experimental temperatures are taken at one radial position in the tank while the computed data are average temperatures on a cross section. Only slight deviations exist at some time intervals, indicating that the basic 1D-2P model has enough accuracy in modeling large-scale packed-bed thermocline tanks. **Fig. 4b** is the comparison on the results of 1D-2P, 1D-3P, and 1.5D-4P models with Sandia pilot-scale packed-bed tank. These simulation curves are not far away from experimental values, but the predicted temperature of 1D-3P and 1.5P-4P models are higher than that of 1D-2P model at a certain height, which may be due to the release of the stored heat in the walls. The phenomenon will be discussed in detail in the following section. By examining the mean difference of different models shown in **Table 4**, it is found that three models show similar standard deviation of around 3 K and two detailed models which can characterize the physical phenomenon in walls show similar root mean square difference of about 5 K, close to that of 1D-2P simple model (4 K). All three models reflect good agreement with the experimental data with an acceptable average difference.

#### 2.3.3. Unification of different scale tanks

Two tanks listed in **Table 1**, the pilot-scale tank (Sandia's Lab) and the hypothetical lab-scale one, will then be fully studied to investigate the wall impact. Despite different sizes and operational temperatures, the influence levels of governing terms should be set similar for better comparison and exploitation. For this purpose, the dimensionless numbers ($\Pi_i$) (**in Eq. S4-S11**) are used to unify two tanks. The dimensionless governing equations of the 1D-3P model **(in Eq. S1-S3)** and corresponding analysis are provided in **Fig. S1** of the Supplementary Data.

## 3. Results and discussion

### 3.1. Wall thermal behavior

#### 3.1.1. General temperature profiles

The 1.5D-4P model was first used to analyze detailed thermal behaviors of fluid and tank walls in discharging. **Figs. 5a and 5b** show the fluid temperature profiles of two tanks along $z$-axial height at different times. Recall that $t_E^*$ is the dimensionless time based on energy flow through the tank, the thermocline zone is defined within the fluid temperature range of $0.05<T^*<0.95$, and the center position of thermocline refers to the height where $T^*=0.5$. At half discharging time ($t_E^*=0.5$), the thermocline

center position of pilot-scale tank is at around $z^*$=0.54, slightly lower than that of the lab-scale tank at $z^*$=0.57. At the same time, in both cases, the thermocline zone is found to be nearly symmetrical, but the thermocline thickness $L^*_{thermocline}$ of pilot-scale tank (0.33) is smaller than that of the lab-scale tank (0.54). All these differences indicate that the pilot-scale tank may have a higher discharging (release) efficiency.

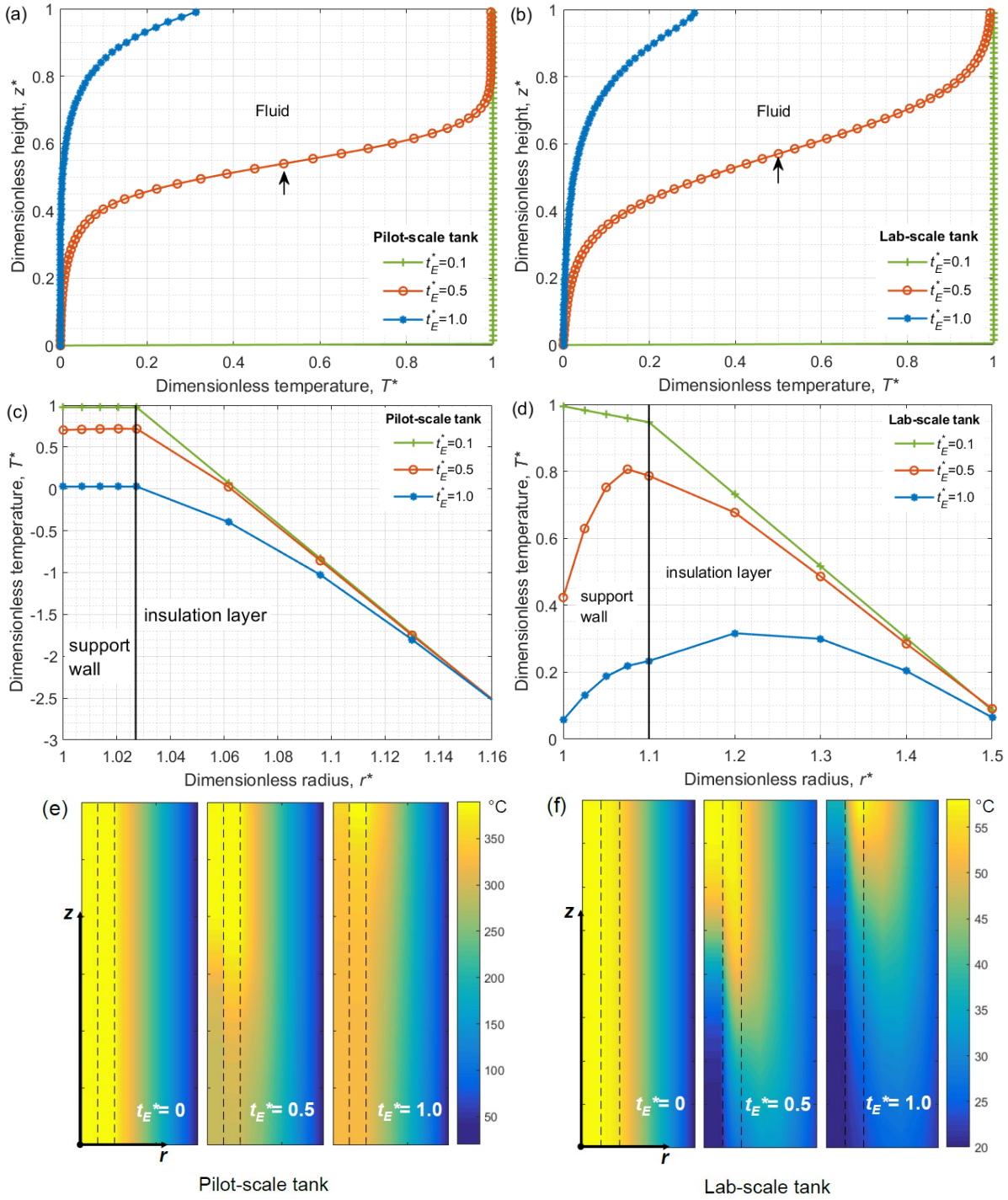

**Fig. 5.** Evolution of temperature profiles of two tanks for the discharging process using 1.5D-4P model. (a) (b) fluid temperature along *z*-axial height; (c) (d) wall and insulation temperature along *r*-direction at the middle tank height ($z^*$=0.5); (e) (f) temperature color map of fluid, wall, and insulation at $t_E^*$=0, 0.5 and 1.

**Figs. 5c and 5d** show temperature distribution of tank walls along the radial direction at the middle tank height ($z^*$ =0.5). **Figs. 5e and 5f** show the cross-sectional temperature color map of three phases. When discharging proceeds, the wall and insulation are cooled down from bottom to top as the cold fluid flows. Note that the insulation temperature $T_{ins}^*$ near the outer surface of the pilot-scale tank shows a negative value due to the far greater cold fluid temperature than the ambient ($T_C \gg T_{amb}$). The variation of $T_w^*$ and $T_{ins}^*$ as a function of $t_E^*$ in the pilot-scale tank shows the same tendency, while for lab-scale tank, the $T_w^*$ shows sharper decrease over the discharging time and there is a heat delay for $T_{ins}^*$. That is because the fluid-wall $Bi_w$ ($Bi_w = \frac{h_{int} \cdot L_w}{\lambda_w}$) is calculated to be 0.1 for pilot-scale tank and be 9 for lab-scale tank. Smaller $Bi_w$ for pilot-scale tank means that heat transfer is mainly governed by convection between wall and fluid, the conduction thermal resistance can thereby be ignored. Furthermore, the dimensionless thermal diffusivity time $t_{diff}^*$ ($t_{diff}^* = \frac{L^2}{\alpha} \cdot \frac{t_E^*}{t}$) is around 0.01 and 2.2 for wall and insulation in pilot scale tank, respectively, and is 0.65 and 2.8 in lab-scale tank. Lower $t_{diff}^*$ shows fast heat transfer speed from wall to fluid. For this reason, $T_w^*$ is almost horizontal at different discharging times in pilot-scale tank.

### 3.1.2. Wall heat flux

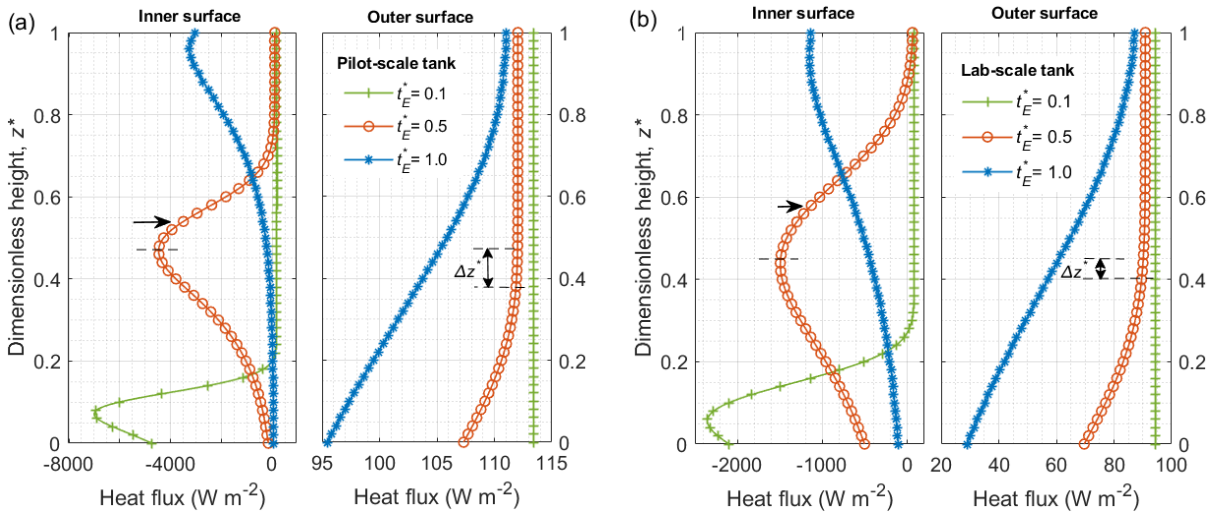


**Fig. 6.** Heat flux at the inner (fluid-wall) and outer (insulation-ambient) surface during the discharging process. (a) pilot-scale tank; (b) lab-scale tank.

Fig. 6 exhibits the heat flux through the wall surfaces based on Fourier's law. At inner (fluid-wall) surface, the negative value of heat flux represents the radial heat transfer from wall to fluid. At outer (insulation-ambient) surface, the positive value indicates the heat flux (heat loss) from the storage tank to the ambient and it reduces with upward fluid flowing. At the beginning of discharging ($t_E^*$=0.1), the inner surface at the top portion of both tanks has a small positive heat flux while the bottom has a larger negative. This is due to the heat loss from the storage tank to the ambient through the top part of tank walls as long as the cold HTF does not reach it. After the arrival of cold fluid, the walls are cooled down and a large proportion of heat initially stored in the tank walls is released back to the fluid, indicated by the negative values of heat flux curves. A small proportion of heat stored in the walls is still dissipated to the ambient, indicated by the always positive values of heat flux through the outer surface of both tanks.

Furthermore, in curves of the inner surface, the peak point of heat flux with the maximum temperature difference between wall and fluid is near the thermocline center, slightly higher than the height of the sharper inflection point of outer surface curve. This height difference ($\Delta z^*$) of thermocline on inner and outer surface reflecting the time delay ($\Delta t_E^*$) is caused by the thermal resistance of wall and

insulation. At the same time, the height difference of lab-scale tank ($\Delta z^* \approx 0.04$) is lower than that of pilot-scale one ($\Delta z^* \approx 0.1$), demonstrating less time to move thermocline on both surfaces due to the lower thermal diffusivity time. Note that the time delay and the height difference are calculated as follows:

**Time delay:** $\Delta t_E^* = t_E^* \ \{z^* = 0.5, \text{peak point of inner surface}\} - t_E^* \ \{z^* = 0.5, \text{sharper inflection point of outer surface}\}$

**Height difference**: $\Delta z^* = z^* \ \{t^* = 0.5, \text{peak point of inner surface}\} - z^* \ \{t^* = 0.5, \text{sharper inflection point of outer surface}\}$

Moreover, the increase of peak span along the z-direction reflects an increment of thermocline thickness over discharging time. The peak height in radial direction decreases over time, due to the smaller wall-fluid temperature difference caused by the continuous heat release from wall to fluid.

### 3.1.3. Wall power analysis

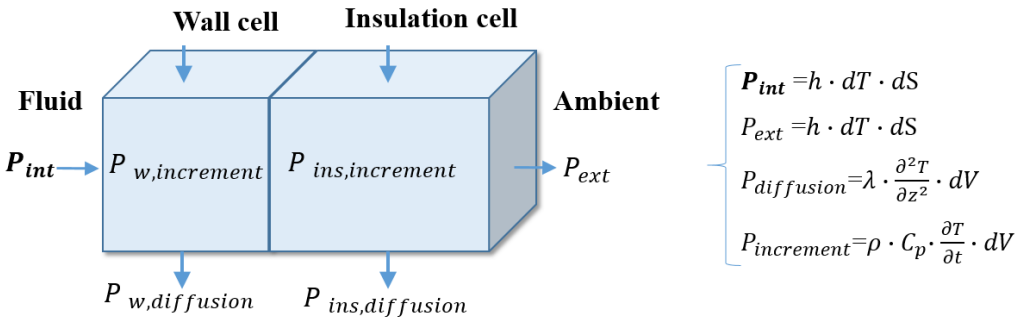


**Fig. 7.** Schematic of power distribution including inner surface convection, wall axial diffusion, insulation axial diffusion, inside increment, and outer surface convection and radiation.

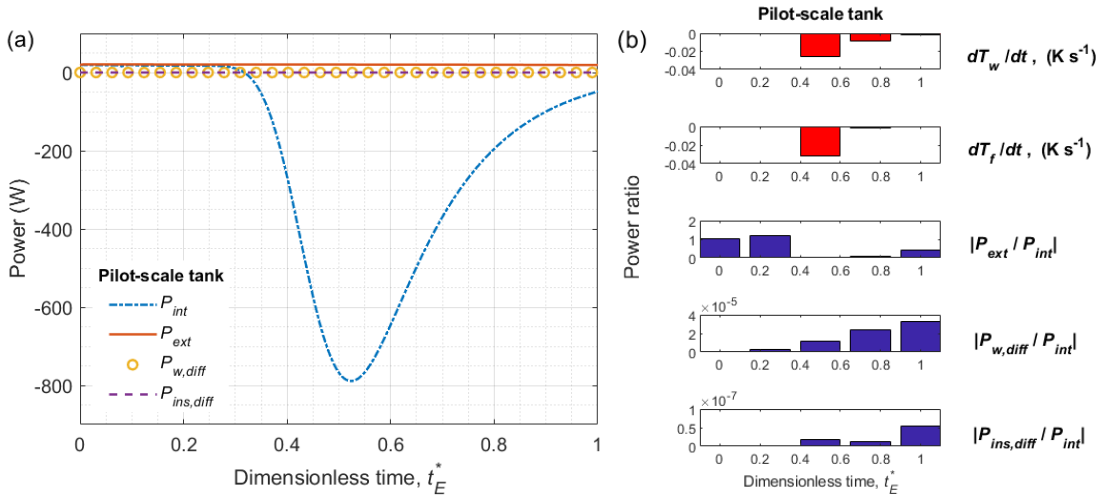

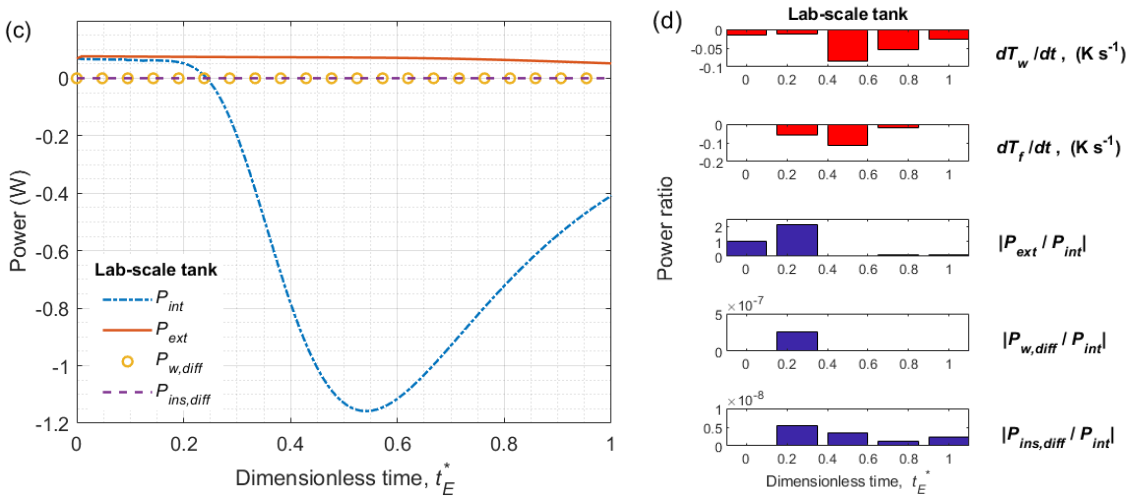


**Fig. 8.** The variation of power over discharging time at middle tank height ($z^*$=0.5). (a), (b) pilot-scale tank; (c), (d) lab-scale tank.

Power analysis of tank walls was conducted to investigate the rate of energy transfer in discharging. **Fig. 7** is the schematic of power distribution through tank walls, including inner surface convection power ($P_{int}$), wall axial diffusion power ($P_{w,diff}$), insulation axial diffusion power ($P_{ins,diff}$), inside increment power ($P_{w,increment} + P_{ins,increment}$), and outer surface convection and radiation power ($P_{ext}$). **Fig. 8** shows the power ratio at the middle height of tank at different discharging times. In this work, each contribution was compared with inner surface input power ($P_{int}$). The $\frac{dT_f}{dt}$ represents the rate of fluid temperature variation at the middle position. At the beginning ($t_E^* = 0.1$), cold flow enters from tank bottom showing a small value of $\frac{dT_f}{dt}$. With time increases to $t_E^* = 0.5$, the thermocline with temperature gradient zone move to the middle height of tank showing a large $\frac{dT_f}{dt}$. The cutoff time, $t_E^* = \text{cutoff}$ referring to the ending time, is a little longer than $t_E^* = 1$. Near the ending time ($t_E^* = 1$), cold fluid fills the tank up showing again a small $\frac{dT_f}{dt}$. A similar tendency can be found for the wall temperature variation rate $\frac{dT_w}{dt}$. Through the results of power ratio, it can be found that the $P_{int}$ is close to the $P_{ext}$ at the beginning. But with the increase of discharging time, $P_{int}$ becomes dominant over other parts. It should be specially noted that the wall and insulation axial diffusion ($P_{w,diff}$ and

$P_{ins,diff}$) are all near 0, indicating that the influence of heat diffusion in axial direction of walls can even be ignored compared to the inner or outer surface heat transfer.

### 3.1.4. Stored heat in wall

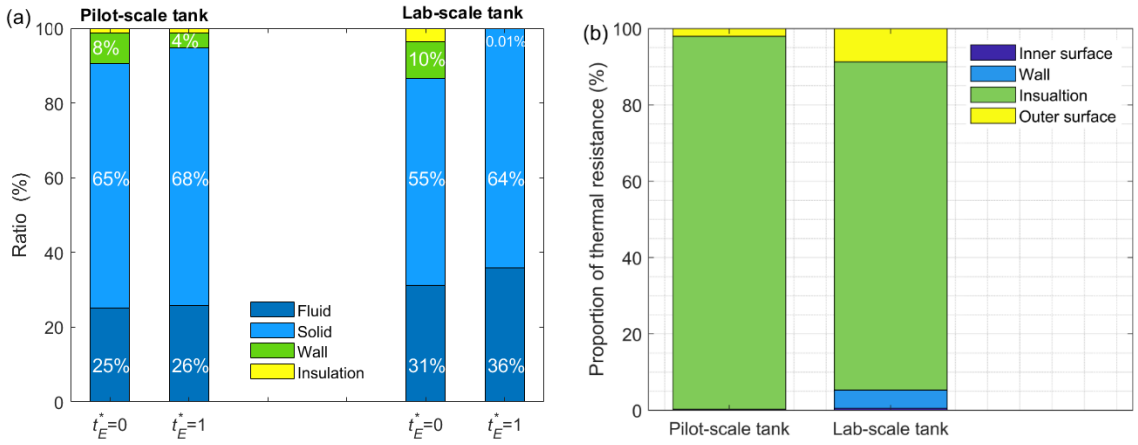


**Fig. 9.** (a) Proportion of stored energy in different phases of packed-bed TES tank at the beginning and $t_E^* = 1$ of discharging; (b) proportion of different thermal resistances at stable heat flux state.

**Table 5**. Values of different HTC for two tanks at average temperature ($T_{ave}$).

| Types | $h_{int}$ (W m$^{-2}$ K$^{-1}$) | $h_{ext}$ (W m$^{-2}$ K$^{-1}$) | $h_{rad}$ (W m$^{-2}$ K$^{-1}$) | $h_o$ (W m$^{-2}$ K$^{-1}$) |
|---|---|---|---|---|
| Pilot-scale tank | 78 | 2.5 | 5.6 | 0.2 |
| Lab-scale tank | 179 | 2.2 | 5.5 | 1.0 |

Fig. 9a shows the percentage of stored energy in each phase at the beginning and of discharging. Before discharging (fully charged state), the solid phase has a dominant energy storage percentage of 65% for lab-scale tank and 55% for pilot-scale tank. The proportion of energy stored in the tank wall is also as high as 8% and 10%, respectively. This non-negligible part of energy remains in fact to be valorized. Nevertheless, the stored energy in the insulation can hardly be captured, implying that the insulation phase may be simplified in the modeling without affecting much the energy efficiency calculation of the packed-bed TES tank. The stored energy ($E_{stored}$) of pilot-scale tank at initial time is around $1\times10^{10}$ J, greatly larger than that of lab-scale tank of around $2\times10^{6}$ J. At $t_E^* = 1$, it decrease to $4\times10^{8}$ J for the pilot-scale tank and $1\times10^{5}$ J for the lab-scale tank. At the cutoff time, energy of each part still decreases and the pump energy due to packed bed pressure drop at cutoff time is $7.3\times10^{3}$ J and 0.24 J, respectively, which can be neglected safely.

**Fig. 9b** shows the contribution of each factor to the total thermal resistance of each tank. The biggest proportion of the total thermal resistance is from the insulation layer. Nevertheless, the heat loss due to radiation should be considered, accounting for about 5% of the total heat loss (lab-scale tank). **Table 5** shows that the lab-scale tank presents higher HTC $h_o$ (1.0 W $m^{-2}$ $K^{-1}$) through the tank walls than that of the pilot-scale tank (0.2 W $m^{-2}$ $K^{-1}$), exhibiting a higher possibility to loss heat to ambient despite a lower value of total heat loss. In summary, the impacts of wall stored energy and radiation heat loss have to be considered in the performance evaluation while the insulation heat capacity and pump energy consumption can be neglected.

### 3.1.5. Energy and exergy efficiency

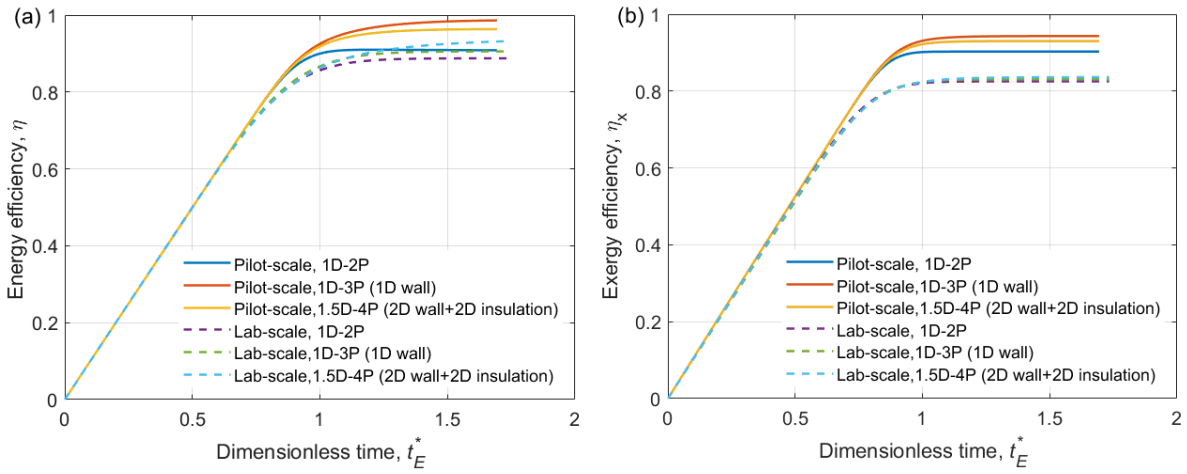


**Fig. 10.** Comparison of (a) energy efficiency and (b) exergy efficiency between 1D-2P, 1P-3P, and 1.5P-4P models for pilot-scale tank and lab-scale tank.

Energy and exergy efficiency variation during discharging and comparison between models based on two indicators are presented in **Fig. 10.** Exergy, as the work potential of energy, is defined as the maximum useful work that can be obtained from system before reaching the equilibrium state [65]. The 100% exergy efficiency refers to completely reversible process and the higher efficiency can be achieved by forming a stable and thinner thermocline or enhanced thermal stratification [66]. It can be observed that energy and exergy efficiencies are time-dependent and show the same increasing tendency for discharging. The energy efficiency at the $t_E^* = 1$ for lab-scale tank (86% using 1D-2P model) is lower than that of the pilot-scale tank (90%), as well as the exergy efficiency. This is because of the higher

heat loss to ambient due to the higher $h_o$ and the more extended thermocline as discussed above. Moreover, it is observed that the difference on exergy efficiency between 1D-3P and 1.5D-4P models is below 5% and both energy higher than 1D-2P model due to the extra heat from wall. Because of complex physical phenomenon description than 1D-2P model and decreased computational time by a factor of 100 than 1.5D-4P model (cf. **Table S1)**, the 1D-3P model can be selected to conduct the wall parameter study.

## 3.2. Wall parametric study

### 3.2.1. The effect of convection and radiation of external surface

**Fig. 11a and b** show the influence of emissivity variation on the tank outer surface temperature, energy and exergy efficiencies. When emissivity changes from a low value of 0.65 to a high value of 0.95, the radiative HTC ($h_{rad}$) increases from 3.8 to 5.6 W m$^{-2}$ K$^{-1}$, causing outer surface temperature to decline and more radiative heat loss to ambient. However, the energy and exergy efficiencies at cutoff time are almost, indicating the tiny influence of emissivity on the overall efficiency of the storage system efficiency.

**Fig. 11b** is the comparison of natural convection and forced convection on the outer surfaces for two tanks. When the effective outdoor HTC (including both convection and radiation) ranges from 17 to 50 W m$^{-2}$ K$^{-1}$ [67], the external HTC ($h_{ext}$) varies from 2 to 17 W m$^{-2}$ K$^{-1}$. This value range considers the heat exchange between the outer surface and the ambient air in real practice [68][69]. The simulation results show the noticeable influence of the external heat transfer coefficient on the evolution of outer surface temperature. Nevertheless, the energy and exergy efficiencies of the storage tank at cutoff time vary slightly by about 0.01% and little influence on the thermocline thickness can be observed.

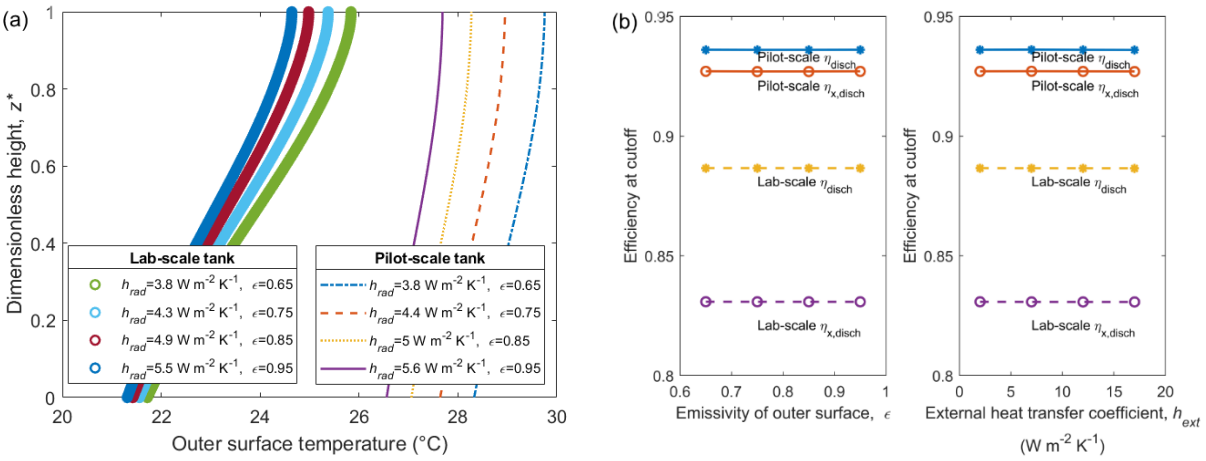


**Fig. 11.** (a) Outer surface temperature at cutoff with emissivity variation; (b) energy and exergy efficiency at cutoff with external heat transfer coefficient variation.

### 3.2.2. The effect of heat stored in wall and heat loss

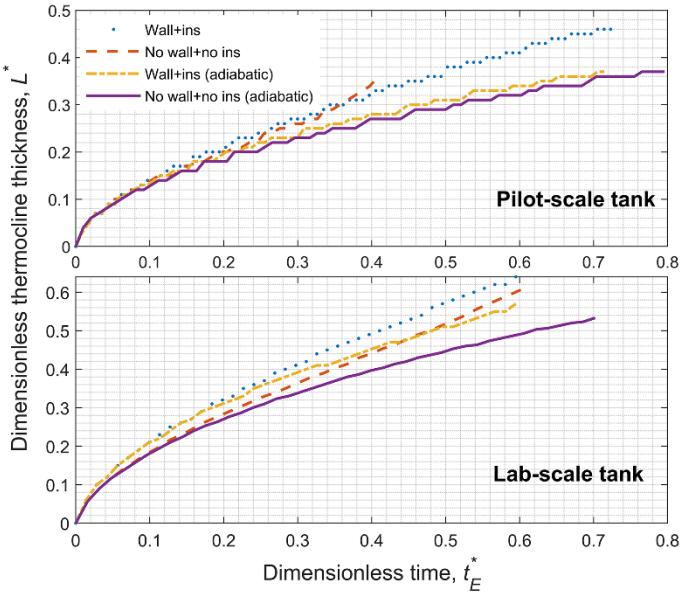


**Fig. 12.** Thermocline thickness variation over discharging time under different boundary conditions of two tanks.

In order to evaluate the influence degree of the wall thermal properties and heat loss on the efficiency of different size tanks, the thermocline thickness over discharging time under different

boundary conditions are investigated, including (1) adiabatic or non-adiabatic and (2) with or without wall and insulation. The ending time was set as when thermocline region reaches the tank top in discharging. **Fig. 12** shows that the thermocline thickness of other three conditions in discharging is always larger than the ideal condition (no wall, no insulation, and adiabatic state), proving that both the stored heat in walls and the heat loss would enlarge the thermocline thickness. Comparing adiabatic conditions of with/without wall and insulation, the degradation of thermocline in the lab-scale tank is more obvious than pilot-scale tank, due to more stored heat of wall returning back to fluid in discharging as explained in earlier sub-sections. Without taking into account of the stored heat in walls and the heat loss, the thermocline thickness might be underestimated by 10% and 15% for pilot-scale tank and for lab-scale tank, respectively.

### 3.2.3. The effect of wall thickness and thermal conductivity

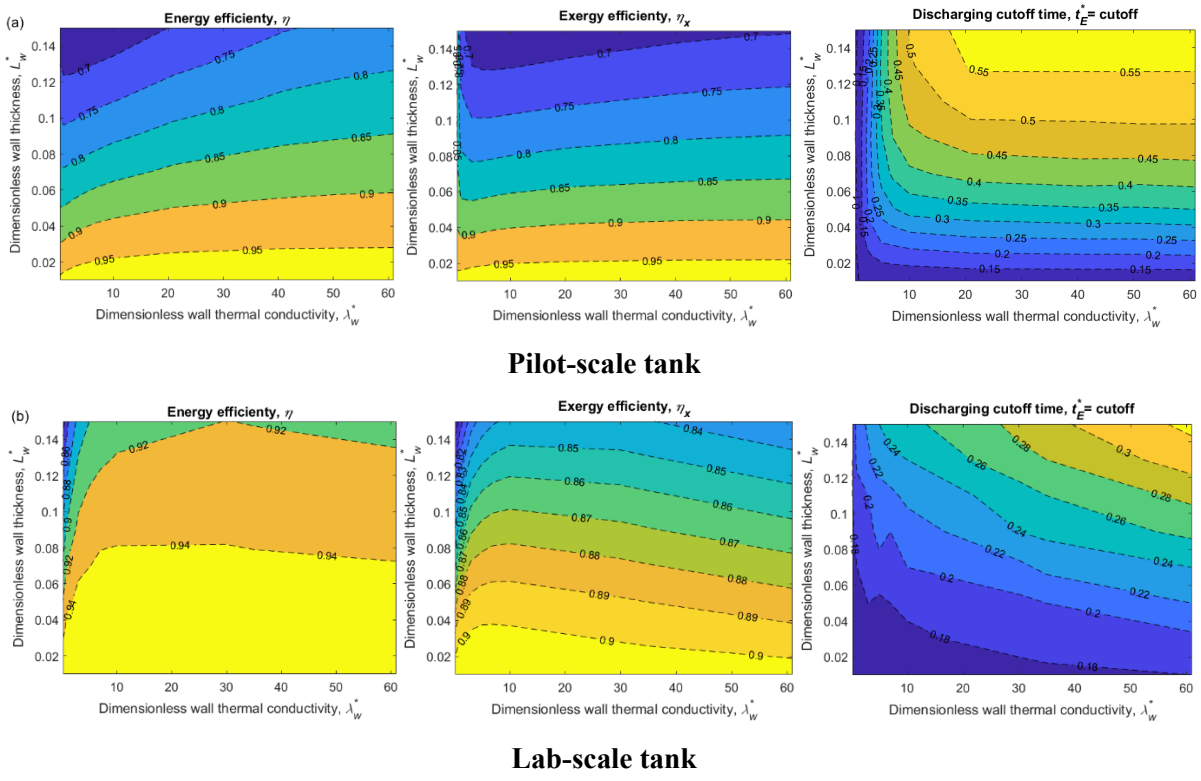


**Fig. 13.** The effect of wall thickness and thermal conductivity on energy efficiency, exergy efficiency and discharging time. (a) pilot-scale tank; (b) lab-scale tank.

The walls parametric study was performed on the wall thermal conductivity and thickness by using the 1D-3P model according to sensitivity analysis in **Fig. S2** of the supplementary data. Three indicators,

including the energy efficiency ($\eta$), the exergy efficiency ($\eta_x$) and the discharging cutoff time, were examined in **Fig. 13**. Recall that $\lambda_w^* = \frac{\lambda_w}{\lambda_f}$ means the ratio of wall thermal conductivity to fluid thermal conductivity ($\lambda_f$), and $L_w^* = \frac{L_w}{R_{int}}$ reflects the ratio of wall thickness to inner radius of fluid region ($R_{int}$). Improving efficiency and decreasing discharging time are the objectives of this parametric study.

At first, the reliable range of the model is proved to be when $\lambda_w^*$>5. Because the $Bi_w$ is low enough in this range that the wall can be served as a 1D, as discussed in detail in **Fig. S3 of the supplementary data**. Then, for both tanks, minimizing the wall thickness can maximize energy and exergy efficiencies (see yellow region) and decrease discharging cutoff time, because a thinner wall means less the initially stored heat of wall according to **Eq.13**. In addition, for pilot-scale tank, the energy and exergy efficiencies decrease with the wall thermal conductivity increases, because the heat exchange rate from wall to fluid improves and the released heat of outlet improves. However, for lab-scale tank, efficiencies decrease with the wall thermal conductivity increase, because the cutoff time is decreased a lot. The wall stored heat increases fluid temperature less for lab-scale tank than the pilot-scale tank. Thus, it was obtained that by a thinner wall thickness causes a smaller impact on energy and exergy efficiency the cutoff time.

## 4. Conclusion

In this work, three models (1D-2P, 1D-3P, and 1.5D-4P) of packed-bed thermocline tank were first developed. After model validation, the wall dynamic thermal behavior was fully investigated and the wall impact on the performance of packed-bed TES tanks has been evaluated. Finally, sensitivity and parametric analyses have been performed using the appropriate 1D-3P model to evaluate the influence of wall parameters. Main findings of this study may be summarized as follows.

(1) Before discharging, the maximum energy stored in wall at fully charged state can be up to 10% of the total stored energy. During discharging, the stored heat in wall can be released back to the fluid, increasing thereby the fluid temperature in contact as well as the thermocline thickness by up to 15%.

(2) The convection heat transfer between fluid and inner wall is dominant while the heat loss from the outer wall to the ambient is time-dependent and non-negligible. In contrast, the axial heat conduction in the walls and the pump power consumption can be ignored.

(3) The stored energy in the insulation is very small. As a result, the insulation phase may be simplified as a thermal resistance in the modeling. In this regard, the 1D-3P model could be a balanced choice between the complex physical phenomenon description and required computational time.

(4) The wall thermal conductivity and thickness have a great impact on wall energy balance, as well as a great interaction degree with other parameters. The optimal wall parameters for packed-bed TES tank is that a thinner wall has a smaller impact on the energy and exergy efficiencies at the discharging cutoff time.

Our on-going work is focused on the packed-bed thermocline TES systems with latent heat storage fillers, which is particularly attractive due to the high energy storage capacity.

## Acknowledgement

This work is supported by the French ANR within the project OPTICLINE (ANR-17-CE06–0013) and by the Chinese Scholarship Council (CSC) with the scholarship for Ms. Baoshan XIE (No. 201908430177).

## References


[1] Rodrigues FA, de Lemos MJS. Effect of porous material properties on thermal efficiencies of a thermocline storage tank. *Appl Therm Eng* 2020;173:115194.

[2] Niedermeier K, Flesch J, Marocco L, Wetzel T. Assessment of thermal energy storage options in a sodium-based CSP plant. *Appl Therm Eng* 2016;107:386–97.

[3] Chang Z, Li X, Xu C, Chang C, Wang Z, Zhang Q, et al. The effect of the physical boundary conditions on the thermal performance of molten salt thermocline tank. *Renew Energy* 2016;96:190–202.

[4] Bataineh K, Gharaibeh A. Optimal design for sensible thermal energy storage tank using natural solid materials for a parabolic trough power plant. *Sol Energy* 2018;171:519–25.

[5] Pelay U, Luo L, Fan Y, Stitou D. Dynamic modeling and simulation of a concentrating solar power plant integrated with a thermochemical energy storage system. *J Energy Storage* 2020;28:101164.

[6] Pardo P, Deydier A, Anxionnaz-Minvielle Z, Rougé S, Cabassud M, Cognet P. A review on high temperature thermochemical heat energy storage. *Renew Sustain Energy Rev* 2014;32:591–610.

[7] Cheng X, Zhai X. Thermal performance analysis of a cascaded cold storage unit using multiple PCMs. *Energy* 2018;143:448–57.

[8] Zaversky F, Pérez de Zabalza Asiain J, Sánchez M. Transient response simulation of a passive sensible heat storage system and the comparison to a conventional active indirect two-tank unit. *Energy* 2017;139:782–97.

[9] Crespo A, Barreneche C, Ibarra M, Platzer W. Latent thermal energy storage for solar process heat applications at medium-high temperatures-A review. *Sol Energy* 2019;192:3–34.

[10] Pelay U, Luo L, Fan Y, Stitou D, Castelain C. Integration of a thermochemical energy storage system in a Rankine cycle driven by concentrating solar power: Energy and exergy analyses. *Energy* 2019;167:498–510.

[11] Mao Q. Recent developments in geometrical configurations of thermal energy storage for concentrating solar power plant. *Renew Sustain Energy Rev* 2016;59:320–7.

[12] Xia L, Zhang P, Wang R. Numerical heat transfer analysis of the packed bed latent heat storage system based on an effective packed bed model. *Energy* 2010;35:2022–32.

[13] Lou W, Luo L, Hua Y, Fan Y, Du Z. A review on the performance indicators and influencing factors for the thermocline thermal energy storage systems. *Energies* 2021;14:8384.

[14] Alva G, Lin Y, Fang G. An overview of thermal energy storage systems. *Energy* 2018;144:341–78.

[15] Cocco D, Serra F. Performance comparison of two-tank direct and thermocline thermal energy storage systems for 1MWe class concentrating solar power plants. *Energy* 2015;81:526–36.

[16] Geissbühler L, Mathur A, Mularczyk A, Haselbacher A. An assessment of thermocline-control methods for packed-bed thermal-energy storage in CSP plants, Part 1: Method descriptions. *Sol Energy* 2019;178:341–50.

[17] Xu C, Li X, Wang Z, He Y, Bai F. Effects of solid particle properties on the thermal performance of a packed-bed molten-salt thermocline thermal storage system. *Appl Therm Eng* 2013;57:69–80.

[18] Galione P, Pérez-Segarra C, Rodríguez I, Torras S, Rigola J. Numerical evaluation of multi-layered solid-PCM thermocline-like tanks as thermal energy storage systems for CSP

applications. *Energy Procedia* 2015;69:832–41.
[19] Zhao B, Cheng M, Liu C, Dai Z. An efficient tank size estimation strategy for packed-bed thermocline thermal energy storage systems for concentrated solar power. *Sol Energy* 2017;153:104–14.
[20] Flueckiger SM, Iverson BD, Garimella S V., Pacheco JE. System-level simulation of a solar power tower plant with thermocline thermal energy storage. *Appl Energy* 2014;113:86–96.
[21] Ortega-Fernández I, Hernández AB, Wang Y, Bielsa D. Performance assessment of an oil-based packed bed thermal energy storage unit in a demonstration concentrated solar power plant. *Energy* 2021;217:119378.
[22] Cascetta M, Cau G, Puddu P, Serra F. A comparison between CFD simulation and experimental investigation of a packed-bed thermal energy storage system. *Appl Therm Eng* 2016;98:1263–72.
[23] Pietruszkiewicz J, Brandon B, Hollenbach R, Lamar M, Smith J, Turchi C, et al. Solar thermocline storage systems: preliminary design study. National Renewable Energy Lab.(NREL), Golden, CO (United States); 2010.
[24] Lou W, Fan Y, Luo L. Single-tank thermal energy storage systems for concentrated solar power: Flow distribution optimization for thermocline evolution management. *J Energy Storage* 2020;32:101749.
[25] Fernández-Torrijos M, Sobrino C, Almendros-Ibáñez JA. Simplified model of a dual-media molten-salt thermocline tank with a multiple layer wall. *Sol Energy* 2017;151:146–61.
[26] Sunku Prasad J, Muthukumar P, Desai F, Basu DN, Rahman MM. A critical review of high-temperature reversible thermochemical energy storage systems. *Appl Energy* 2019;254:113733.
[27] Díaz-Heras M, Belmonte JF, Almendros-Ibáñez JA. Effective thermal conductivities in packed beds: Review of correlations and its influence on system performance. *Appl Therm Eng* 2020;171:115048.
[28] Argo WB, Smith JM. Heat transfer in packed beds-prediction of radial rates in gas-solid beds. *Chem Eng Prog* 1953;49:443–51.
[29] De Beer M, Du Toit CG, Rousseau PG. Experimental study of the effective thermal conductivity in the near-wall region of a packed pebble bed. *Nucl Eng Des* 2018;339:253–68.
[30] Yagi S, Wakao N. Heat and mass transfer from wall to fluid in packed beds. *AIChE J* 1959;5:79–85.
[31] Yang Z, Garimella S V. Molten-salt thermal energy storage in thermoclines under different environmental boundary conditions. *Appl Energy* 2010;87:3322–9.
[32] Mira-Hernández C, Flueckiger SM, Garimella S V. Comparative analysis of single- and dual-media thermocline tanks for thermal energy storage in concentrating solar power plants. *J Sol Energy Eng Trans ASME* 2015;137.
[33] Beasley DE, Clark JA. Transient response of a packed bed for thermal energy storage. *Int J Heat Mass Transf* 1984;27:1659–69.
[34] Xu C, Wang Z, He Y, Li X, Bai F. Sensitivity analysis of the numerical study on the thermal performance of a packed-bed molten salt thermocline thermal storage system. *Appl Energy* 2012;92:65–75.
[35] Hoffmann JF, Fasquelle T, Goetz V, Py X. A thermocline thermal energy storage system with filler materials for concentrated solar power plants: Experimental data and numerical model sensitivity to different experimental tank scales. *Appl Therm Eng* 2016;100:753–61.

[36] Bellan S, Gonzalez-Aguilar J, Romero M, Rahman MM, Goswami DY, Stefanakos EK, et al. Numerical analysis of charging and discharging performance of a thermal energy storage system with encapsulated phase change material. *Appl Therm Eng* 2014;71:481–500.
[37] Opitz F, Treffinger P. Packed bed thermal energy storage model - Generalized approach and experimental validation. *Appl Therm Eng* 2014;73:245–52.
[38] Cascetta M, Serra F, Arena S, Casti E, Cau G, Puddu P. Experimental and numerical research activity on a packed bed TES system. *Energies* 2016;9:1–13.
[39] ELSihy ElsS, Liao Z, Xu C, Du X. Dynamic characteristics of solid packed-bed thermocline tank using molten-salt as a heat transfer fluid. *Int J Heat Mass Transf* 2021;165:120677.
[40] Wu M, Xu C, He YL. Dynamic thermal performance analysis of a molten-salt packed-bed thermal energy storage system using PCM capsules. *Appl Energy* 2014;121:184–95.
[41] Çengel YA, Ghajar AJ. Heat and mass transfer: fundamentals and applications. McGraw Hill Education; 2020.
[42] Ranmode V, Singh M, Bhattacharya J. Analytical formulation of effective heat transfer coefficient and extension of lumped capacitance method to simplify the analysis of packed bed storage systems. *Sol Energy* 2019;183:606–18.
[43] Bradshaw A V, Johnson A, McLachlan NH, Chiu YT. Heat transfer between air and nitrogen and packed beds of non-reacting solids. *Trans Inst Chem Eng Chem Eng* 1970;48:T77–84.
[44] Xu B, Li PW, Chan CL. Extending the validity of lumped capacitance method for large Biot number in thermal storage application. *Sol Energy* 2012;86:1709–24.
[45] Wakao N, Kaguei S, Funazkri T. Effect of fluid dispersion coefficients on particle-to-fluid heat transfer coefficients in packed beds. Correlation of nusselt numbers. *Chem Eng Sci* 1979;34:325–36.
[46] Kaguei S, Shiozawa B, Wakao N. Dispersion-concentric packed bed heat. *Chem Eng Sci* 1976;32:507–13.
[47] Deissler RG, Boegli JS. An investigation of effective thermal conductivities of powders in various gases. *Trans Am Soc Mech Engrs* 1958;80:1417–23.
[48] Gonzo EE. Estimating correlations for the effective thermal conductivity of granular materials. *Chem Eng J* 2002;90:299–302.
[49] Yang B, Bai F, Wang Y, Wang Z. Study on standby process of an air-based solid packed bed for flexible high-temperature heat storage: Experimental results and modelling. *Appl Energy* 2019;238:135–46.
[50] Pfeffer R. Heat and mass transport in multiparticle systems. *Ind Eng Chem Fundam* 1964;3:380–3.
[51] Stuke B. Berechnung des Wärmeaustausches in Regeneratoren mit zylindrischem und kugelförmigem Füllmaterial. *Angew Chemie* 1948;20:262–8.
[52] Staff V-GV und C. VDI-wärmeatlas. Springer Berlin Heidelberg; 2006.
[53] Ergun S. Fluid flow through packed columns. *Chem Eng Prog* 1952;48:89–94.
[54] Prieur du Plessis J, Woudberg S. Pore-scale derivation of the Ergun equation to enhance its adaptability and generalization. *Chem Eng Sci* 2008;63:2576–86.
[55] Chang Z, Li X, Xu C, Chang C, Wang Z. The design and numerical study of a 2 MWh molten salt thermocline tank. *Energy Procedia* 2015;69:779–89.
[56] Bayón R, Rojas E. Simulation of thermocline storage for solar thermal power plants: From dimensionless results to prototypes and real-size tanks. *Int J Heat Mass Transf* 2013;60:713–21.

[57] Flueckiger SM, Yang Z, Garimella S V. Thermomechanical simulation of the solar one thermocline storage tank. *J Sol Energy Eng Trans ASME* 2012;134:041014.
[58] Fass SE. 10 MWe solar thermal central receiver pilot plant: thermal storage subsystem evaluation-final report. *SAND86-8212, Sandia Natl Lab Albuquerque, New Mex* 1986.
[59] Douglas M. 10 MWe solar thermal central receiver pilot plant mode 5 (test 1150) and mode 6 (test 1160) test report. *Sandia Natl Lab SAND86-8175* 1986.
[60] Pacheco J, Showalter S. Development of a molten-salt thermocline thermal storage system for parabolic trough plants. *J Sol Energy Eng* 2002;124:153–9.
[61] Molina S, Haillot D, Deydier A, Bedecarrats JP. Material screening and compatibility for thermocline storage systems using thermal oil. *Appl Therm Eng* 2019;146:252–9.
[62] Zhao B, Cheng M, Liu C, Dai Z. System-level performance optimization of molten-salt packed-bed thermal energy storage for concentrating solar power. *Appl Energy* 2018;226:225–39.
[63] Shaikh W, Wadegaonkar A, Kedare SB, Bose M. Numerical simulation of single media thermocline based storage system. *Sol Energy* 2018;174:207–17.
[64] Esence T, Bruch A, Molina S, Stutz B, Fourmigué JF. A review on experience feedback and numerical modeling of packed-bed thermal energy storage systems. *Sol Energy* 2017;153:628–54.
[65] Bejan A, Tsatsaronis G, Moran MJ. Thermal design and optimization. John Wiley and Sons; 1995.
[66] Bindra H, Bueno P, Morris JF, Shinnar R. Thermal analysis and exergy evaluation of packed bed thermal storage systems. *Appl Therm Eng* 2013;52:255–63.
[67] Chartered Institution of Building Services Engineers(CIBSE). Thermal properties of building structures in: K.J. Butcher (Ed.), GuideA: Environmental Design, 7th ed., Norwich: 2006, p. 5–48.
[68] Howell JR, Menguc MP, Siegel. R, Siegel R. Thermal radiation heat transfer. Boca Raton, FL, USA: National Aeronautics and Space Administration; 1964.
[69] Incropera FP, Lavine AS, Bergman TL, Dewitt DP. Fundamentals of heat and mass transfer. New York: Wiley; 2007.

# Supplementary data

# Wall impact on efficiency of packed-bed thermocline thermal energy storage system

Baoshan XIE[1], Nicolas BAUDIN[1], Jérôme SOTO[1,2], Yilin FAN[1], Lingai LUO[1,*]

[1]*Nantes Université, CNRS, Laboratoire de thermique et énergie de Nantes, LTeN, UMR 6607, F-44000 Nantes, France*

[2]*Institut Catholique d'Arts et Métiers de Nantes, 35 avenue du Champ de Manœuvres, 44470 Carquefou, France*

## S1. Definition of dimensionless numbers

In order to solve the model with different parameters, the governing equations of 1D-3P model are nondimensionalized into:

$$\left(\frac{\partial T_f^*}{\partial t^*}+\frac{\partial T_f^*}{\partial z^*}\right)=\Pi_1\cdot\frac{\partial}{\partial z}\cdot\left(\frac{\partial T_f^*}{\partial z^*}\right)+\Pi_2\cdot\left(T_s^*-T_f^*\right)+\Pi_3\cdot\left(T_w^*-T_f^*\right) \tag{S1}$$

$$\frac{\partial T_s^*}{\partial t^*}=\Pi_4\cdot\frac{\partial}{\partial z^*}\cdot\left(\frac{\partial T_s^*}{\partial z^*}\right)+\Pi_5\cdot\left(T_f^*-T_s^*\right) \tag{S2}$$

$$\frac{\partial T_w^*}{\partial t^*}=\Pi_6\cdot\frac{\partial}{\partial z^*}\cdot\left(\frac{\partial T_w^*}{\partial z^*}\right)+\Pi_7\cdot\left(T_f^*-T_w^*\right)+\Pi_8\cdot\left(T_{amb}^*-T_w^*\right) \tag{S3}$$

$$\Pi_1=\frac{1}{Pe}\frac{\lambda_{f,eff}}{\lambda_f}\frac{D_p}{H} \tag{S4}$$

$$\Pi_2=St_{sf,eff}a_sH \tag{S5}$$

$$\Pi_3=St_{f-w}a_fH \tag{S6}$$

$$\Pi_4=\frac{1}{Pe}\frac{\varepsilon}{(1-\varepsilon)}\frac{\alpha_{s,eff}}{\alpha_f}\frac{D_p}{H} \tag{S7}$$

$$\Pi_5=St_{sf,eff}a_sH\frac{\rho_fC_{p,f}}{\rho_sC_{p_s}}\frac{\varepsilon}{(1-\varepsilon)} \tag{S8}$$

$$\Pi_6=\frac{1}{Pe}\varepsilon\frac{\alpha_w}{\alpha_f}\frac{D_p}{H} \tag{S9}$$

$$\Pi_7=St_{sf,eff}a_wH\frac{\rho_fC_{p,f}\varepsilon}{\rho_wC_{p_w}} \tag{S10}$$

$$\Pi_8=St_{w-amb}a_wH\frac{\rho_fC_{p,f}\varepsilon}{\rho_wC_{p_w}} \tag{S11}$$

where,

$$Pe = Re \cdot Pr = \frac{D_p \cdot u_{sup}}{\alpha_f} \quad \text{(S12)}$$

$$St = \frac{Nu}{Re \cdot Pr} = \frac{Nu}{Pe} \quad \text{(S13)}$$

$$\alpha = \frac{\lambda}{\rho \cdot C_p} \quad \text{(S14)}$$

In definition, $\Pi_i$ reflect the energy contribution to each phase. For example, $\Pi_1$, $\Pi_4$, and $\Pi_6$ represent the influence of the ratio of heat diffusion to increment term on energy, while $\Pi_2$, $\Pi_3$, $\Pi_5$, $\Pi_7$, and $\Pi_8$ represent the influence of ratio of the heat convection plus radiation to increment term on energy.

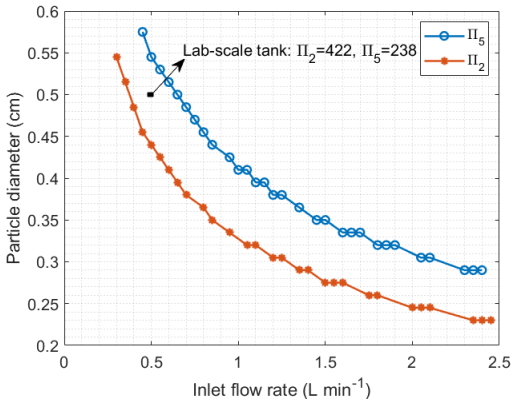


**Fig. S1.** The dominant dimensionless number of $\Pi_2$ and $\Pi_5$ of the lab-scale tank at the certain fluid interfacial velocity and particle diameter is near to the pilot-scale tank ($\Pi_2$=525, $\Pi_5$=201).

In order to set two tanks at a similar resolution condition, the $\Pi_i$ were calculated and compared. Here, for the pilot-scale tank with a certain packing configuration, the $\Pi_2$ and $\Pi_5$ are dominant. Therefore, a comparison of both tanks can thus be conducted under the condition that the value of dominant $\Pi_i$ of two tanks is determined to be close to each other in **Fig. S1**.

# S2. Computational time needed busing different models

**Table S1** Computational time of 1D-2P, 1D-3P, and 1.5D-4P model at cutoff time*.

| Models | Computation time (s) | | |
|---|---|---|---|
| | 1D-2P model | 1D-3P model (1D wall+1D insulation) | 1.5D-4P model (2D wall+2D insulation) |
| Pilot-scale tank | 5 | 8 | 833 |
| Lab-scale tank | 9 | 10 | 606 |

*The processor of the modeling computer is: Intel Processeur Xeon CPU E5-2609 @2.40GHz.

## S3. Parametric sensitivity analysis

To better understand the effect of different parameters on the performance of the storage tank, especially the wall impact, global sensitivity analysis (GSA) was conducted by using the 1D-3P model. An adaptation algorithm named the Morris method, or Elementary Effect (EE) method, which gives rough quantitative estimations with a limited number of calculations, was used based on a MATLAB toolbox provided by Pianos [S1]. It computes two sensitivity indices for each input: one is the mean of EEs, measuring the effect of an input over output, and another is the standard deviation of EEs, representing the interaction degree with other factors. In this study, the main parameters ($\varepsilon, u_{v,f}, D_p, \lambda_s, L_w, \rho_s C_{p_s}, \lambda_w, \rho_w C_{p_w}$) were served as input after considering the determined tank geometry size and HTF type. The $\Pi_i$ in dimensionless energy equation were taken as outputs, which reflect the contribution of the heat convection, the convection, or the radiation on fluid, solid, and wall energy. The definition has been introduced in **Eqs. S4-11**.

**Table S2** Value range of parameters for sensitivity analysis.

| Parameters | Symbols | Units | Ranges | |
|---|---|---|---|---|
| | | | Pilot-scale tank | Lab-scale tank |
| Particle diameter | $D_p$ | cm | 0.2-1.0 | 0.2-1.0 |
| Porosity | $\varepsilon$ | -- | 0.2-0.4 | 0.2-0.4 |
| Mass flow rate*[1] | $\dot{m}_f$ | kg $s^{-1}$ | 3-10 | $8.3\times10^{-3}$-$24.8\times10^{-3}$ |
| Wall thickness*[2] | $L_w$ | cm | 4-15 | 0.3-1.0 |
| Wall thermal conductivity | $\lambda_w$ | W $m^{-1}$ $K^{-1}$ | 0.2-60 | 0.2-60 |
| Wall volumetric heat capacity*[3] | $\rho_w C_{p_w}$ | J $m^{-3}$ $K^{-1}$ ($\times10^5$) | 15-66 | 15-66 |
| Solid thermal conductivity | $\lambda_s$ | W $m^{-1}$ $K^{-1}$ | 0.1-35 | 0.1-35 |
| Solid volumetric heat capacity*[3] | $\rho_s C_{p_s}$ | J $m^{-3}$ $K^{-1}$ ($\times10^5$) | 15-66 | 15-66 |

*1 Mass flow rate for both tanks are determined according to the similar interfacial velocity range.

*2 Wall thickness for both tanks are determined according to the similar ratio range (wall thickness/tank height).

*2 Volumetric heat capacity for solid and wall are located in range between the low (like glass or plastic) and high value (like metals).

**Table S3** Dimensionless number ($\Pi_i$) variation within the value range of parameters.

| Dimensionless number | Pilot-scale tank | Uncertainty | Lab-scale tank | Uncertainty |
|---|---|---|---|---|
| $\Pi_1$ | $5\times10^{-4}$ | $\pm 4\times10^{-4}$ | $8\times10^{-3}$ | $\pm 5\times10^{-3}$ |
| $\Pi_2$ | 4000 | $\pm 3\times10^{4}$ | 243 | ± 1790 |
| $\Pi_3$ | 1 | ± 1 | 1 | ± 1 |
| $\Pi_4$ | $2\times10^{-4}$ | $\pm 10\times10^{-4}$ | $4\times10^{-3}$ | $\pm 10\times10^{-3}$ |
| $\Pi_5$ | 14000 | ± 35000 | 120 | ± 1380 |
| $\Pi_6$ | $10\times10^{-4}$ | $\pm 8\times10^{-4}$ | $14\times10^{-3}$ | $\pm 80\times10^{-3}$ |
| $\Pi_7$ | 2 | ± 14 | 3 | ± 15 |
| $\Pi_8$ | $22\times10^{-4}$ | ± 0.2 | $14\times10^{-3}$ | $\pm 70\times10^{-3}$ |

For different operation conditions or packing configurations, the parametric sensitivity analysis within the variable ranges of parameters was studied. The value range of parameters is indicated in **Table S2** and the corresponding dimensionless number variation is reported in **Table S3**. For both tanks, the influence of heat convection ($\Pi_2$, $\Pi_5$) on the performance of storage tank is larger than heat loss ($\Pi_3$, $\Pi_7$, $\Pi_8$), while the influence of axial conduction ($\Pi_1$, $\Pi_4$, $\Pi_6$) can be largely ignored. This is in line with our findings reported above. Samples number is defined as 4000 according to the convergence result shown in **Fig. S2 a and b.**

The dominant $\Pi_i$ ($\Pi_2$, $\Pi_5$, $\Pi_7$ and $\Pi_8$) for each phases all own to heat convection. $\Pi_7$ have dominant influence on wall energy balance due to the wall impact on heat loss of lab-scale tank. Thus, **Fig. S2 c and d** displays the means and standard deviation of EEs of main parameters for $\Pi_7$ of two tanks. It demonstrated that wall volumetric heat capacity, wall thickness, and wall thermal conductivity have a great impact on wall energy balance, as well as a great interaction degree with other parameters. Considering the wall volumetric heat capacity is the inherent property of material, the wall parameters only containing wall thickness and wall thermal conductivity be studied in this study.

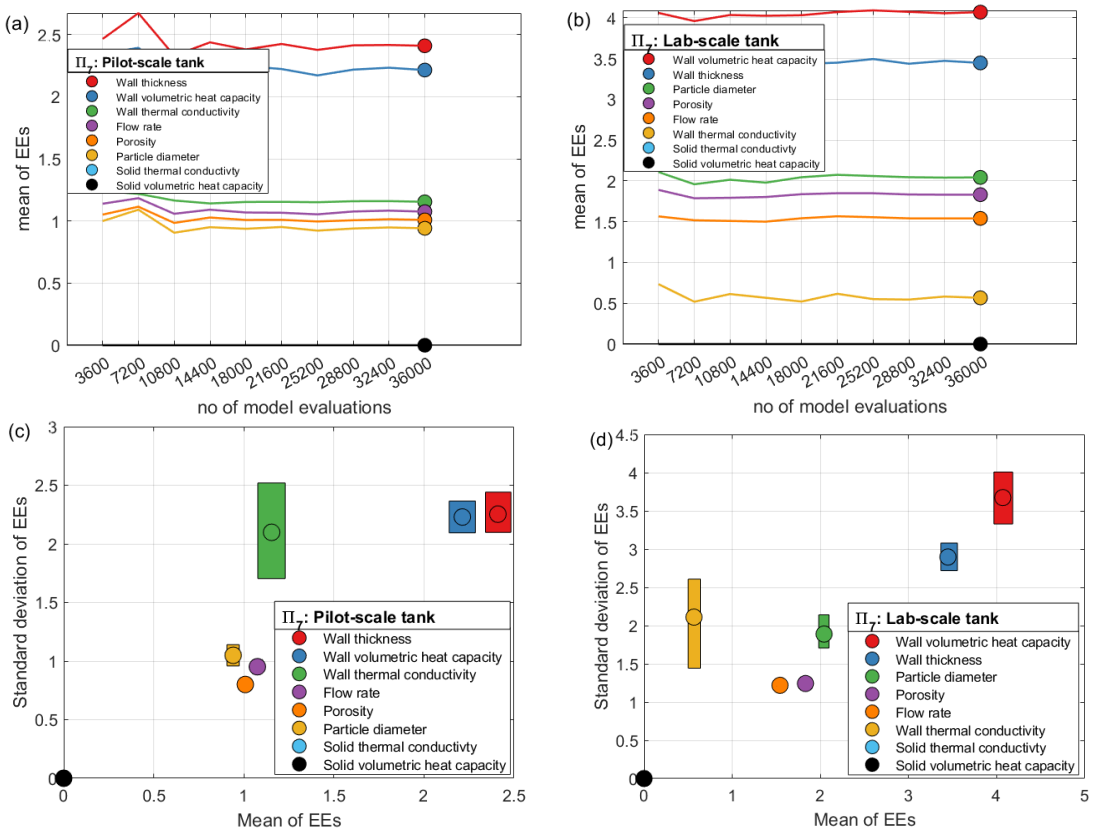


**Fig. S2.** Sensitivity analysis: convergence results of dominant dimensionless number $\Pi_7$ (a), (b); elementary effect method of $\Pi_7$ (c), (d).

# S4. Variation of wall-to-fluid Biot number

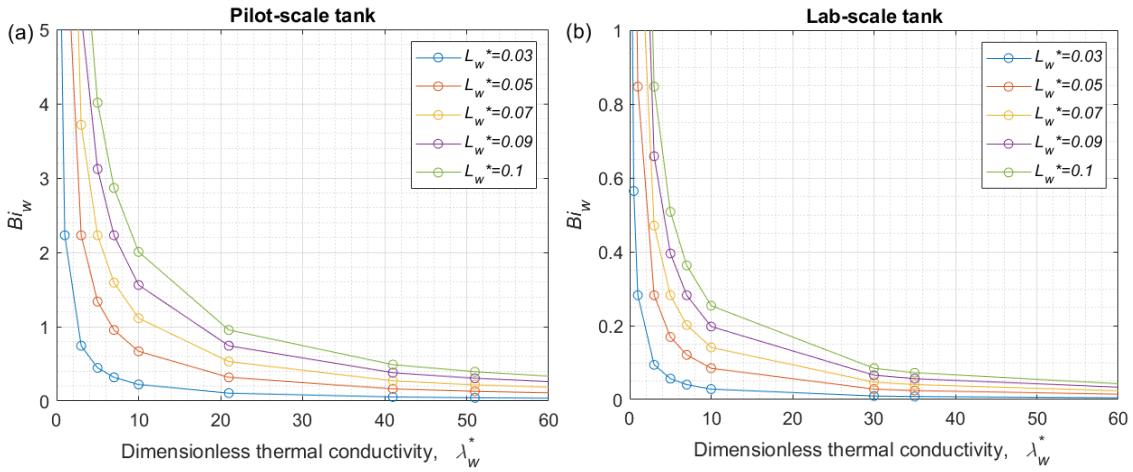


**Fig. S3.** Wall-to-fluid Biot number ($Bi_w$) variation with the change of wall thermal conductivity and dimensionless wall thickness: (a) pilot-scale; (b) lab-scale tank.

**Fig. S3** shows the variation of $Bi_w$ with the change of two variables: the wall thermal conductivity and the dimensionless wall thickness. The $Bi_w$, a ratio of thermal resistance of the inside wall and inner surface of wall, can reflect the reliability of the model at relatively low value (especially $Bi_w$<0.1). As it shows, the $Bi_w$ increases sharply when $\lambda_w^*$<5. Thus, the inflection point near $\lambda_w^*$=5 can be used as a threshold value that the model results is validated.

## Reference

[S1] Pianosi F, Sarrazin F, Wagener T. A Matlab toolbox for Global Sensitivity Analysis. *Environ Model Softw* 2015;70:80–5.